GENETIC PROGRAMMING IN DESIGNING ADVANCED METAMATERIAL ABSORBERS

A THESIS SUBMITTED TO THE GRADUATE DIVISION OF THE UNIVERSITY OF HAWAIʻI AT MĀNOA IN PARTIAL FULFILLMENT OF THE REQUIREMENTS FOR THE DEGREE OF

MASTER OF SCIENCE

IN

ELECTRICAL ENGINEERING

DECEMBER 2022

By
Edmond C.M. Chong

Thesis Committee:

Magdy F. Iskander, Chairperson
Zhengqing Yun
Yuanzhang Xiao

Keywords: metamaterials, absorbers, graphene

This thesis is dedicated to my parents,

Alex Chong and Sandy Lin, for pushing me

to achieve great things and supporting me

throughout my journey.

ACKNOWLEDGMENTS

I want to thank my advisor, Dr. Magdy F. Iskander, for his passion for teaching electromagnetics. His enthusiasm in his classes stuck with me, which led me to pursue my research at the Hawaii Advanced Wireless Technologies Institute (HAWTI). I would also like to thank him for introducing me to a new world of electromagnetics which consists of metamaterials. I was utterly oblivious to metamaterials until I joined HAWTI, and I am glad I could contribute, pushing the envelope of what is available.

I want to thank the support from Raytheon Technologies and their new co-sponsored fellowship in engineering electromagnetics.

I would also like to thank the Combat Capabilities Development Command Chemical Biological Center for technical oversight.

I would also like to thank Dr. Zhengqing Yun and Dr. Yuanzhang Xiao for agreeing to serve on my thesis committee and providing feedback during our weekly meetings.

I would also like to thank Dr. Akhlesh Lakhtakia for his helpful discussions on the characterizations of single-layer graphene.

I would also like to thank Scott Clemens for teaching me everything I know today about genetic programming and Dr. Gui Chao Huang for helping me out whenever I was in a pinch.

I also thank my great friends Christopher Leong, Blake Wong, and Sunny Zhang for their constant moral support. We would constantly bounce ideas off of each other, bettering each other's projects along the way.

Finally, I want to thank my sister Wendy Chong for helping me along every step of the way and giving me words of encouragement so I would never falter.

ABSTRACT

Metamaterials are artificial materials that possess properties otherwise not found in nature. The current state of metamaterial absorbers (MMA) in the lower gigahertz frequency (1-11 GHz) is sparse and commonly resides in the X-band (8-12 GHz). Typical 2D MMA have topologies designed by trial and error and are either compact with discrete operational frequencies or bulky and lossy to achieve broadband performance. Hybrid genetic programming (HGP) is proposed to create new compact design topologies in the lower gigahertz frequency with new material development. HGP can create new topologies optimized per input parameters, such as low frequency and high broadband absorptivity. These designs are built and simulated in Ansys High-Frequency Simulation Software (HFSS) and evaluated by HGP. Additional topologies, such as graphene and resistive sheet patterning, and resistive sheet insert, are explored and implemented with HGP to create compact, low-gigahertz frequency and high-absorptivity MMAs. The graphene-based and resistive sheet-based patterned designs achieved 80% bandwidth above 80% absorptivity from 4.6 to 11 GHz, up to 15 GHz, and from 3.83 to 9.13 GHz, respectively. Preliminary measurements of a fabricated resistive sheet insert design aligned with simulated results.

TABLE OF CONTENTS

LIST OF TABLES

LIST OF FIGURES

SYMBOLS, ACRONYMS, AND ABBREVIATIONS

ϵ	Permittivity
ϵ_o	Permittivity of Free Space
ϵ_r	Relative Permittivity
$\hbar$	Reduced Planck's constant
λ	Wavelength
$\mathcal{E}$	Energy
μ_c	Chemical Potential
ω	Operation Frequency
σ	Conductivity
σ_0	Complex Surface Conductivity Intra-band Contributions
σ_s	Complex Surface Conductivity
τ	Electro-phonon Relaxation Time
E_{dc}	Electric Field Bias
$F(\mathcal{E})$	Fermi-Dirac Distribution
k_B	Boltzmann's Constant
q_e	Electron Charge
S_{11}	Reflection Coefficient
S_{21}	Transmission Coefficient
T	Temperature
v_F	Fermi Speed of Graphene
A	Absorptivity
tan δ_e	Dielectric Loss Tangent

AMC Artificial Magnetic Conductor

FDTD Finite-Difference Time-Domain

GA Genetic Algorithm

GP Genetic Programming

HAWTI Hawaii Advanced Wireless Technologies Institute

HFSS High Frequency Simulation Software

HGP Hybrid Genetic Programming

IR Infrared

L-system Lindenmayer System

LIG Laser-Induced Graphene

MATLAB Matrix Laboratory

MMA Metamaterial Absorber

PEC Perfect Electric Conductor

RAL Radar Absorbing Layer

RLC Resistor, Inductor, Capacitor

CHAPTER 1
INTRODUCTION

1.1 Background

Metamaterials are artificial materials that possess properties otherwise not found in nature. Metamaterials typically consist of subwavelength periodic structural unit cells. A unit cell usually is composed of three layers—a metallic pattern and a dielectric spacer, followed by a metallic backplane. The metallic planar patterns create resonant frequencies with each other. The patterned layer can be tuned to match the impedance of the surrounding free space, achieving zero reflections at the surface. The dielectric substrate spacer is to disperse the incoming wave, but that does not come without a cost. The dielectric medium contains losses, and when it disperses the incoming wave, it is gets converted to heat energy. Including the metallic backplane, the transmission of the incoming wave is rendered to zero. Metamaterial impedance surfaces are designed surfaces such that the design dictates reflection and transmission [6]. Metamaterial absorbers (MMA), a subset of metamaterial impedance surfaces, ranging from microwave, infrared, visible, and terahertz spectrum, have been researched and developed for ”thermophotovoltaics, photodetection, bolometry, and manipulation of mechanical resonances” [7].

This project's design parameter of interest is broadband absorption in the low gigahertz frequency range (1-11 GHz). Typical MMA designs for the microwave regime exist in the X band (8-12 GHz) or higher. These designs consist of a metal-dielectric-metal design, where the top layer is a metal pattern and the bottom layer is a metal backplate. These designs create resonating structures that increase the electric field at the surface and have discrete high narrow absorption peaks. Several methods broaden the absorption frequency range [8]; one method combines the multiple absorption peaks by combining multiple resonant structures [9]. Another includes stacking resistive sheets between the dielectric layer [4] or stacking multiple metal and dielectric layers and shaping them into pyramids [10]. Another method is to include lumped elements into the design to match the impedance of free space. Designs that achieve lower frequency absorption are bulky designs with lossy material or multiple layers of stacked dielectrics with a high profile. Lossy materials in the metamaterial design will generate heat when absorbing the incoming radar waves. Although the device will be invisible in the radar spectrum, heating will continue to show in the infrared spectrum. Using low-loss materials will circumvent the amount of generated heat but not wholly.

Multispectral absorptivity has been achieved by stacking radar MMA and IR emission shielding [11]. The multispectral metamaterial is designed to pass incoming radar waves through the IR shielding layer, are absorbed by the radar absorber, and thermal energy is emitted into the 3-5 μm band.

Flexible metamaterials have become of great interest as they can conform to different shapes and sizes. Most common metamaterials consist of rigid structures based on the materials used in the design. A visible light transparent flexible metamaterial was proposed that achieved broadband absorption from 8-17 GHz and IR emissivity less than 0.3 from 3-14 μm [12]. There is still room for improvement to lower the frequency range of this proposed structure. Material selection is highly emphasized in multispectral designs as the material properties dictate how well a design will perform [7].

Broadband absorbers are preferred as they cover a broader frequency range, but this does not come with its limitation on the device. Broadband is achieved by coupling multiple resonances determined by the pattern on the top layer [7]. Another method to broaden the bandwidth is to include multiple layers of different dielectrics—one thing to note is that the thickness of the absorber is directly promotional to the largest operating wavelength [4]. An example of this limitation is that single-frequency absorbers can be designed to be where thin, less than a quarter wavelength [3], while broadband absorbers are bulky [10]. Basic shapes such as squares, circles, and crosses are used in the patterning for metamaterial absorbers and emitters [4].

Most MMA resides in the X band of 8-12 GHz. 2D planar patterns have been used primarily for metamaterials as they are relatively easy and cheap to fabricate. There needs to be a simple solution for fabricating 3D metamaterials. Including 3D geometries suspended in the dielectric medium is challenging while maintaining the resolution of the geometries needed for resonances.

Multispectral metamaterials combine microwave and infrared or infrared and optical regimes. However, few combine all three, where it is a metamaterial that is optically transparent, can absorb incoming radar waves, and dissipate the absorbed energy into the infrared spectrum [11][13][14].

Metallic-based patterned MMAs rely on the resonance of the pattern. These designs create unstable surface impedances at broadband frequencies, leading to narrow bandwidths. The metal pattern can be replaced by tunable material to create a relatively stable surface impedance [15]. Graphene is greatly sought for its excellent electrical properties and conductivity tunability [16]. Resistive sheets come in all shapes and sizes, and resistive values to use to create a stable impedance surface for broadband performance.

Computational methods create metamaterial designs and provide insight into how the device will perform before being fabricated. The equivalent circuit method creates an equivalent circuit of the metamaterial design where capacitance and inductances replicate the electromagnetic characteristics of the design and resistances replicate the losses in the design [17]. Multiple RLC circuits are used to model the coupling paths of a design. Transmission line models were used to model the characteristic impedance and length of the dielectric medium of a unit cell [18]. So far, the equivalent circuit method is extensively used in 2D metamaterials but needs more research in 3D metamaterials.

Another method for metamaterial design is digital-based metamaterials, where each unit cell within an array of unit cells can map to a 1-bit 0 or 1. A simple structure where 0 represents 0 degrees in phase, and 1 represents 180 degrees in phase [19]. More bits can be added to increase the phase gradient across at metasurface by changing the size of the metallic patch on top of the dielectric. Different implementations of the digital coding metamaterials method are showcased in [20]. One notable design is where a 2-bit metasurface has each information mapped to 16 different top layer patterns instead of scaling the size of the pattern.

Another method for metamaterial design is genetic programming (GP) and genetic algorithm (GA) to create and optimize the designs to meet design parameters. A hybrid GP was used with a low-level GA optimizer to synthesize 3D artificial magnetic conductor (AMC) topologies [1]. The GP software takes in user-design parameters and automatically creates an initial population of designs via a tree-based data structure. These designs are automatically modeled as unit cells and simulated in the Ansys High-Frequency Simulation Software (HFSS). The phase and reflection magnitude is evaluated against a user-defined fitness function. Designs with the best (lowest) fitness score will be used to create the next set of design populations through elitism, crossover, and mutation. The GP software will iterate and optimize designs until the user-defined parameters are met.

Another method for creating metamaterial designs is the fractal method, Lindenmayer systems or L-systems. The L-system creates fractal designs with a string of instructions. As the iteration increases, the fractal design becomes more apparent. The L-system has been incorporated into the GP software [21]. The L-system was used to create drawing instructions for the generated designs. These metamaterial designs created are unique and otherwise not created by human expertise.

As new materials are considered for metamaterial designs, not all available materials have electrical properties readily available. As metamaterials become thinner to reduce bulk and increase compact profile, the electrical properties of known materials might behave differently at thinner sizes. In [22], they developed a metalized ceramic coaxial probe that can measure the dielectric properties of thin samples using Finite-Difference Time-Domain (FDTD) software. A perfect electrical conductor is proposed to be placed behind the thin sample as it replicates laboratory measurements consistent with the FDTD model. Although it is stated that any material with know properties will work too. A coaxial probe is modeled on top of a thin sample and simulated in the FDTD software at various thicknesses and varying complex permittivity. The measured input impedance of the thin sample is referenced against the different thicknesses' complex permittivity to determine the measured sample's complex permittivity.

Testing of metamaterials is needed to validate simulation results. Metamaterials in the microwave regime are tested in an anechoic chamber. In the anechoic chamber, a transmitter, receiver horn antenna, and network analyzer are used to measure the reflection and phase of the metamaterial design structure. The transmitter sends a signal down to the metamaterial, and the receiver picks up the reflected signal. Figure 1.1 shows the testing of a fabricated metamaterial absorber in the Hawaii Advanced Wireless Technologies Institute (HAWTI) anechoic chamber.

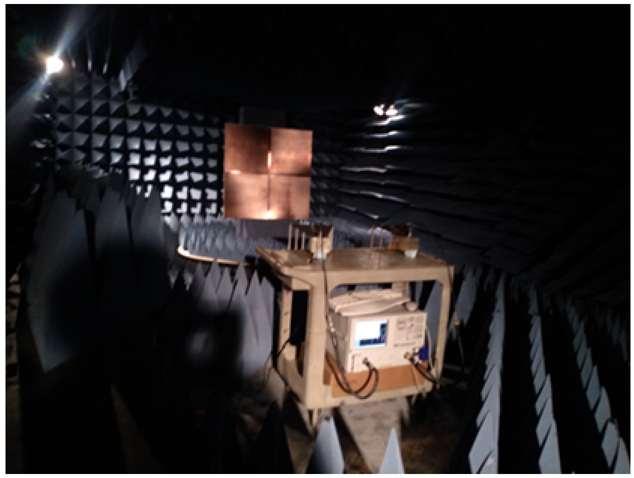

Figure 1.1: Anechoic chamber for the measurement of metamaterial properties

GP was used to create two 3D AMC metamaterial designs from 225 MHz to 450 MHz [1]. The designs consisted of multilayer dielectrics and planar metallic wire patterns between the layers of dielectrics. The planar wire pattern within the design is a single wire wrapped around the unit cell, forming a single wire when combined with neighboring unit cells. Multiple planar-wrapped wires can exist in a single design and span between the different dielectric layers. The length of the planar wires in these 3D designs directly correlates to the low-frequency performance of the AMC. Figure 1.2 shows one of the 3D AMC designs created by GP with multilayer dielectrics and metallic planar wires. Difficulty fabricating 3D metamaterials has limited the experimental validation of these 3D AMC metamaterial designs.

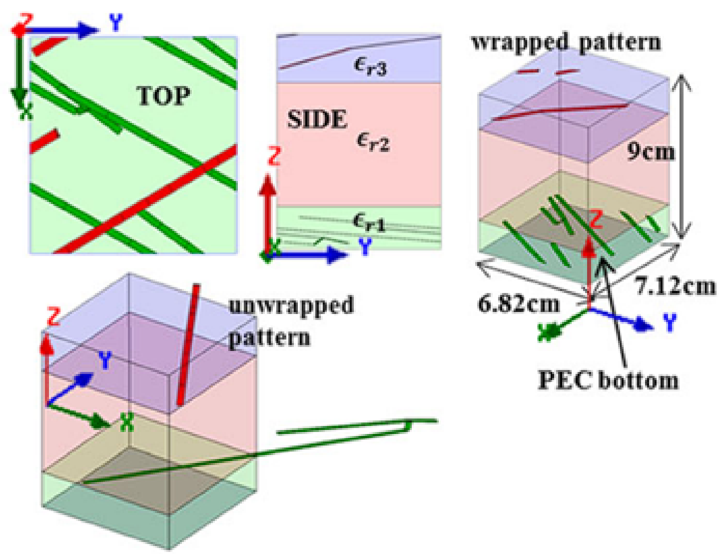

Figure 1.2: GP 3D AMC with multilayer dialectics and two sets of planar metallic wires [1]

GP was also used to create 2D AMC metamaterials. They designed and simulated 2D metamaterial AMC and showcased how the GP AMC outperforms other literature AMCs [2]. GP was unleased using the same dielectric substrate parameters of literature designs to create new topologies that outperform the literature results regarding reflection magnitude and phase performance. Figure 1.3 shows a GP AMC topology outperforming the literature design in bandwidth while retaining the same phase performance. A couple of the 2D metamaterial AMC designs created from GP were fabricated in [23]. These fabricated 2D AMCs were measured in an anechoic chamber, and the experimental results matched the simulated results. Equivalent circuit modes and Prony's method were developed to understand how these complex topologies created by GP outperform those of human expertise [18].

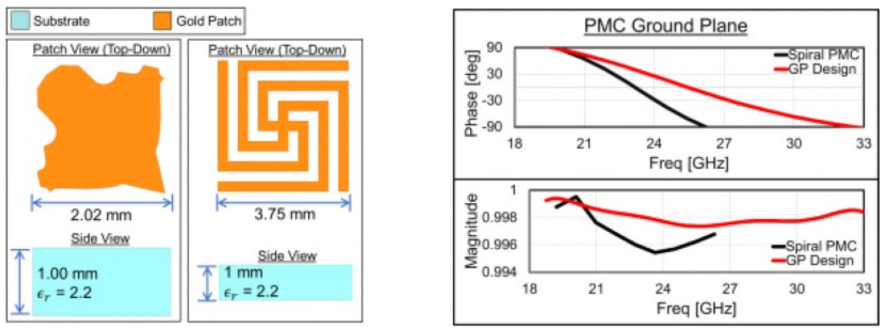

Figure 1.3: GP AMC topology outperforming literature spiral design [2]

1.2 Objective

As electromagnetic technology develops, single-frequency or multiple-frequency operational absorbers cannot keep up in the complex electromagnetic environment [15]. There is an opportunity to present a solution that addresses broadband MMAs in the low gigahertz frequency range. The research presented in this thesis aims to solve this design challenge by implementing different methods to broaden the frequency range while creating compelling designs for fabrication. The objective of this research follows:

- Use of Genetic Programming software to design MMAs at low gigahertz frequencies (1-11 GHz), using 2D/3D patterning, and PEC bottom.
- Exploring new materials, graphene, and resistive sheet materials together with Genetic Programming for broadband performance

1.3 Contributions

- Demonstrating that Genetic Programming can generate broadband metamaterial structures in the challenging lower frequency range (1-11 GHz)
- Application of Genetic Programming with graphene and resistive sheet material
- Provide designs for graphene and resistive sheet patterning

1.4 Organization of Thesis

Chapter 2 covers the simulation process in building the unit cell used in simulations and simulations of literature designs to validate the simulation process. Chapter 3 presents the methodology for implementing GP in MMA designs and some preliminary results using GP. Chapter 4 presents the use of graphene as patterned material, the characterization of graphene conductivity, and addresses the challenges of using laser-induced graphene. Chapter 5 presents resistive sheets as an alternative material to graphene and initial testing and experimental verification of using a resistive sheet. Conclusions and future work are presented in Chapters 6 and 7, respectively. Finally, supplemental material is included in the appendices, Appendix A includes the function used to characterize graphene conductivity, and Appendix B includes a list of published publications.

CHAPTER 2
SIMULATION PROCESS

2.1 Building Unit Cell

Metamaterials presented consist of periodic subwavelength structures called unit cells. The unit cell for metamaterials is modeled and simulated in Ansys High-frequency Simulation Software (HFSS). The substrate material is modeled and characterized by electrical properties such as permittivity, permeability, and loss tangent. On top of the substrate layer is the metallization pattern; it is modeled using geometric shapes as 2D sheets, and it is assigned as perfect electrical conduction (PEC). Below the substrate is a metallic ground plane, modeled as a 2D sheet and assigned as a PEC. The whole structure is surrounded by an air box at least $\lambda/4$ tall. Figure 2.1 show an example of a unit cell modeled in HFSS. The sides of the airbox are assigned with master and slave boundaries, and the top is assigned with a floquet port. The floquet port allows the unit cell to be simulated as an infinite array. A frequency sweep is assigned to the model to be analyzed. Within the frequency range, a wide range of points can be discretely solved, or the points can be interpolated. The design is then verified within HFSS and analyzed to obtain the S parameters. HFSS builds a mesh for the model and solves matrix operations to solve for the S parameters.

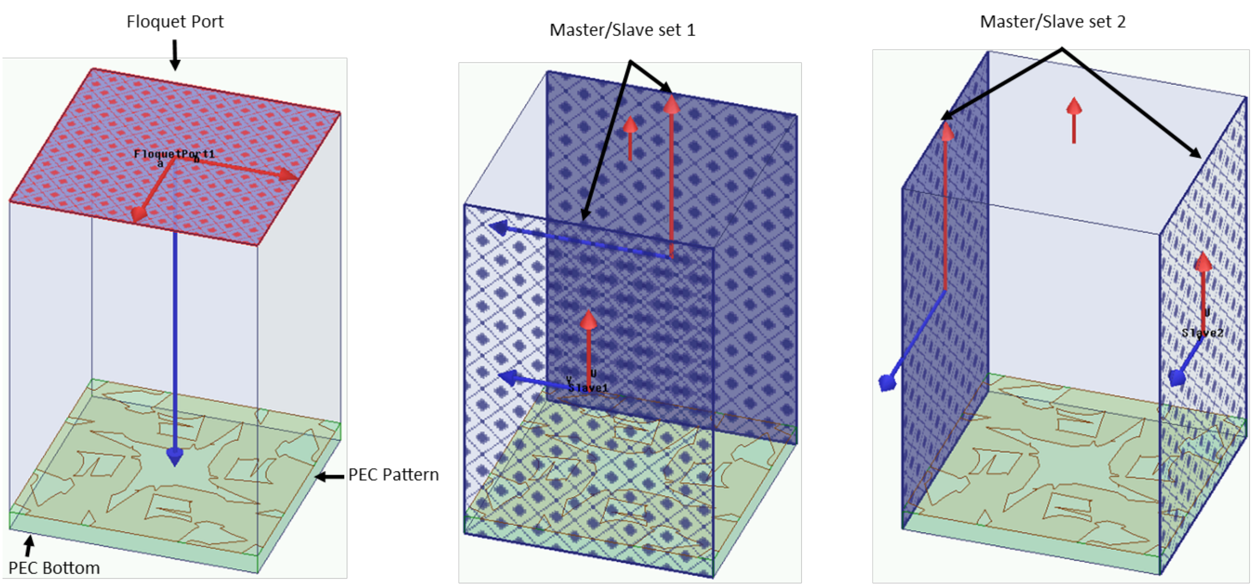

Figure 2.1: Setup of HFSS model for metamaterial unit cell

2.2 Simulating Literature Designs

Literature designs were modeled and simulated in HFSS to validate HFSS simulation methodologies and literature results. The simulating literature design parameters give insight into the design input parameters for GP. Figure 2.2 shows the design of a radar-absorbing layer (RAL) with two discrete peaks above 90% absorptivity at 6.38 and 8.47 GHz [3]. The design consists of a square border with a cross copper pattern on top of FR4, backed with a copper backplane. Figure 2.3 shows the design of a broadband absorber consisting of stacked dielectric foam with resistive sheets embedded in between the dielectric foam [4]. The absorptivity of this design is above 90%, from 2.33 to beyond 10 GHz.

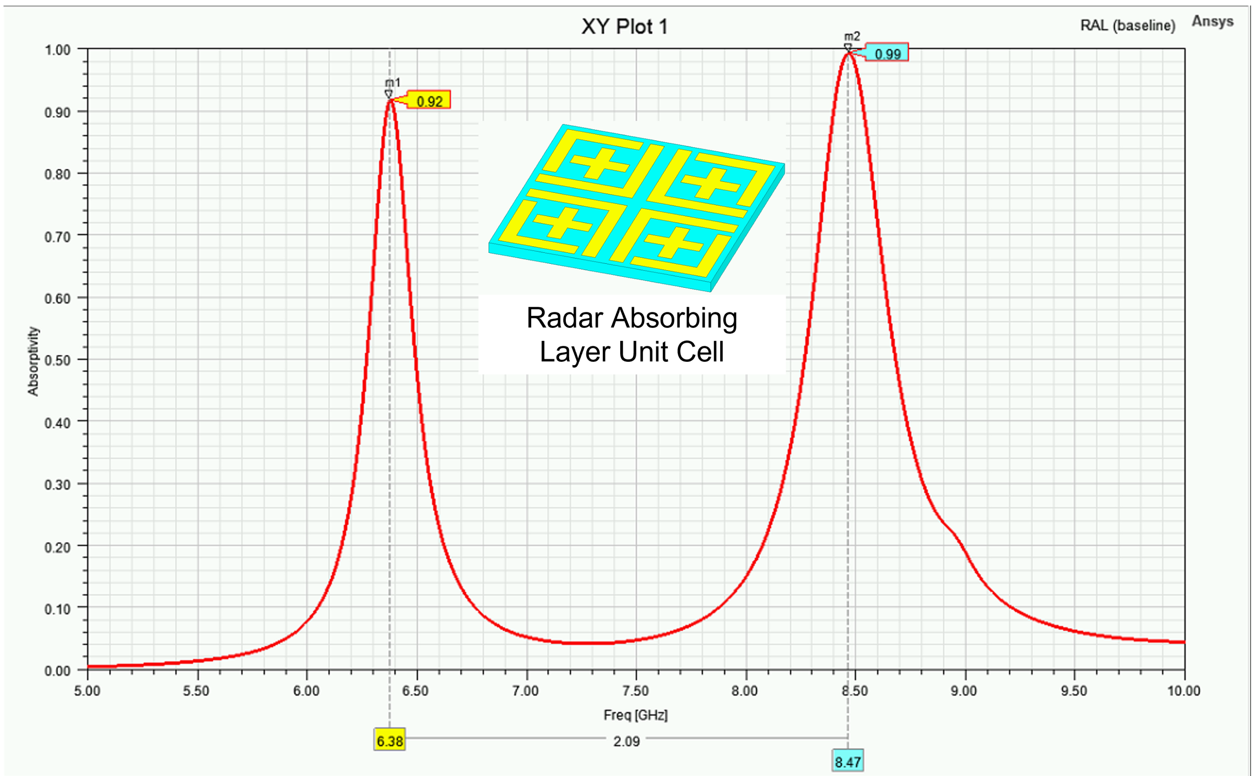

Figure 2.2: RAL design with two discrete absorptivity peaks above 90% at 6.38 GHz and 8.47 GHz [3]

The simulation of these two designs informs the different structures GP can simulate. Either single-layer dielectric substrates with metalization on top or multilayer dielectrics with embedded sheets. With GP, new designs can be combined with metallic patterns on top of multilayer dielectric substrates with embedded sheets.

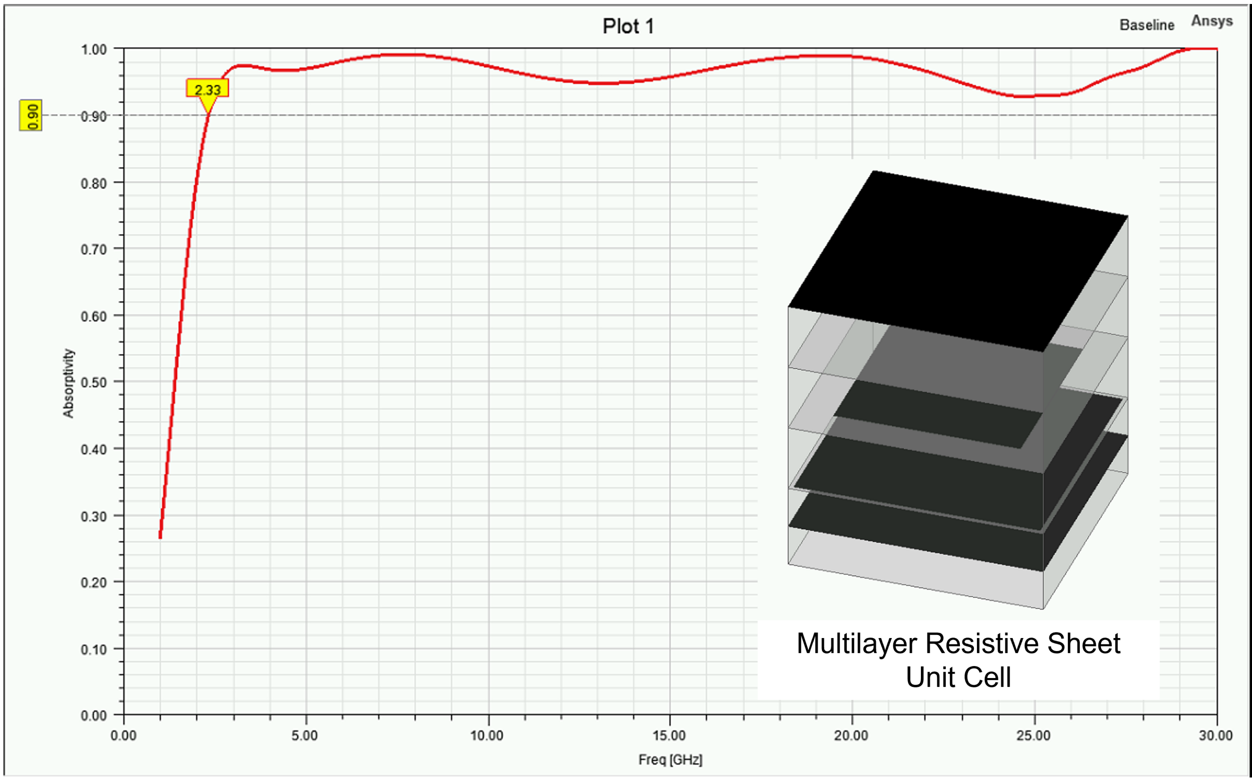

Figure 2.3: Multilayer resistive sheet design with broadband absorptivity above 90% from 2.33 GHz to beyond 30 GHz [4]

2.2.1 Scaling Unit Cell

Scaling the unit cell is a method that can lower the resonant frequency of given designs. The length of a design is linearly proportional to the frequency used to measure the design [24]. Figure 2.4 shows the frequency decrease when the unit cell for the radar-absorbing layer is scaled up by two compared to the original scale. The radar-absorbing layer with absorptivity peaks at 6.4 GHz was lowered to 3.18 GHz, and the 8.4 GHz peak was lowered to 4.16 when doubled in size. Figure 2.5 shows the improved bandwidth of the scaled design compared to the original size. The multi-dielectric design with embedded resistive sheets obtained sub GHz performance from 2 GHz when tripled in size, but at 12 GHz, the absorptivity drops below 0.6. The size of the scaled device informs what range of values to use as initial parameters for GP to obtain resonant frequencies in the lower GHz frequency bands.

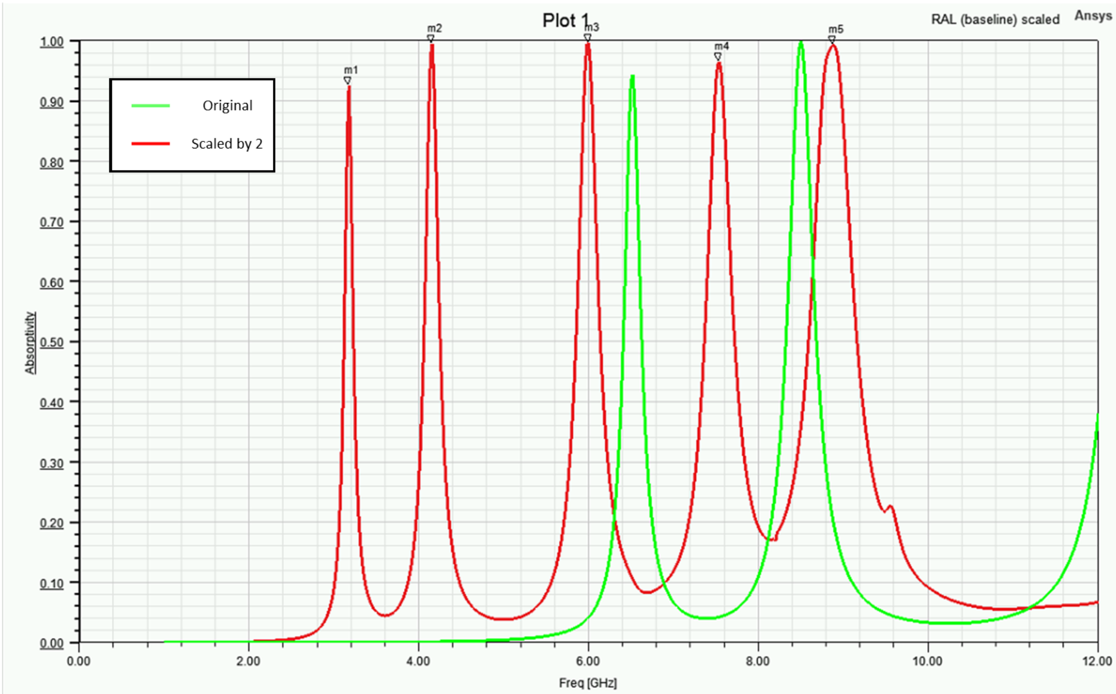

Figure 2.4: Lower frequency absorptivity peaks when scaled up by two compared to original scale [3]

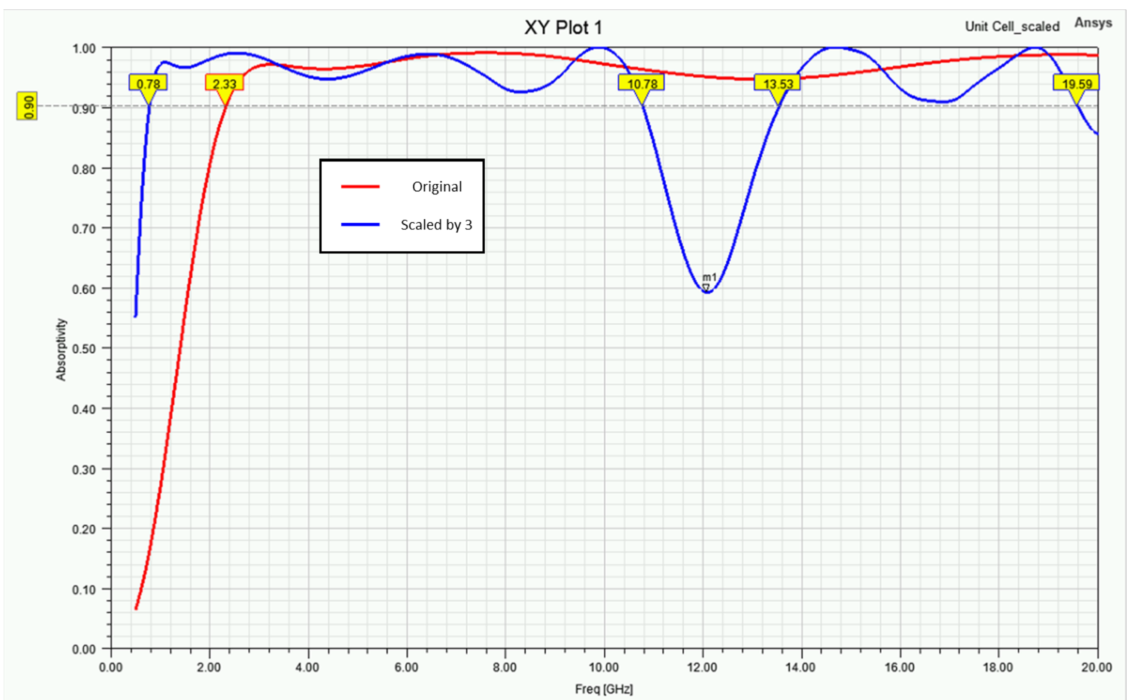

Figure 2.5: Sub GHz lowest operational frequency when scaled up by three, but absorptivity drops at 12 GHz compared with original scale [4]

CHAPTER 3
GENETIC PROGRAMMING

3.1 Methodology

Hybrid genetic programming (HPG) is a combination of genetic programming (GP) with a low-level genetic algorithm (GA) optimizer. GP is utilized to create new design topologies and optimize design parameters. The low-level GA optimizer is used to improve the optimization efficiency of the design parameters.

GP is a biological evolution-inspired algorithm where genetic operations are applied to a population over generations to design new topologies with high-performance characteristics. GP creates an initial population of designs and will evaluate this population's performance through a fitness function. A tree structure represents each member of the population, and the nodes represent operations or design parameters. Genetic-based operations are applied to the best-performing designs and will create the next set of populations of designs. The genetic-based operations are crossover, mutation, and elitism. Crossover mixes the design parameters of two members to create a new member, and mutation randomly changes one of the design parameter values to create a new member. Elitism pass along the best-performing member to the next population. The design parameter trees consist of the substrate tree and the pattern tree. The substrate and pattern tree assign values for the unit cell to be modeled in HFSS. The substrate tree assigns values for the substrate's dimensions and electrical properties. The pattern tree creates patterns from a closed polygon based on a floating number of vertices. Each vertice is connected through a straight line or a cubic spline. Figure 3.1 shows various lines, splines, and vertices that will "draw" a pattern and create a new topology for the unit cell.

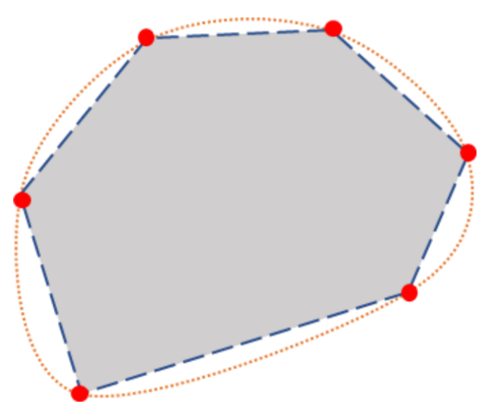

Figure 3.1: Polygon generation from various vertices (red), cubic splines (orange), and straight lines (blue) [5]

An initial set of parameter range values are used to determine the initial population of designs. These parameter values include unit cell dimensions, substrate material selection, and pattern topology. The designs created by HGP are simulated in Ansys HFSS. HGP interfaces with HFSS via a script file created in MATLAB. The HFSS script file contains instructions to model the unit cell, run the simulation, and export the data. The unit cell is modeled and simulated in an infinite array. The S parameter data is exported back to MATLAB to be evaluated against the fitness function. The fitness function for absorption follows absorptivity, A, the fraction of the amount of incident electromagnetic waves absorbed by the surface. Where A is:

$$A = 1 - S_{11} - S_{21} \tag{3.1}$$

Where S_{11} and S_{21} are the reflectivity and transmissivity, respectively, the reflectivity is defined by the magnitude squared of the reflection coefficient, the S_{11} parameter, and the transmissivity is defined by the magnitude squared of the transmission coefficient, the S_{21} parameter. Although the designs have a metallic backplane, the S_{21} parameter is from the floquet port used in the full-wave simulations. The inclusion of the S_{21} parameter is to exclude any designs that have cross-polarization.

Once the designs are evaluated, the top (lower fitness scores) designs will have the genetic operations applied. GP will create the next generation of populations where GP optimizes unit cell dimensions, pattern topology, and substrate material. As the number of generations increases, the fitness score converges to a design that meets the criteria of high broadband absorption.

A flow chart for the methodology of HGP between MATLAB and HFSS is shown in figure 3.2. The initial parameters are inputted and used to create the initial population of designs. A script file is created based on the population of designs and sent to be modeled and simulated in HFSS. Parallelization is implemented to run multiple simulations simultaneously. The designs are evaluated and sent to the low-level optimizer, and genetic operations are applied and simulated in parallel. The designs are evaluated and sent back to GP. Genetic operations are applied once again to create the next generation of populations.

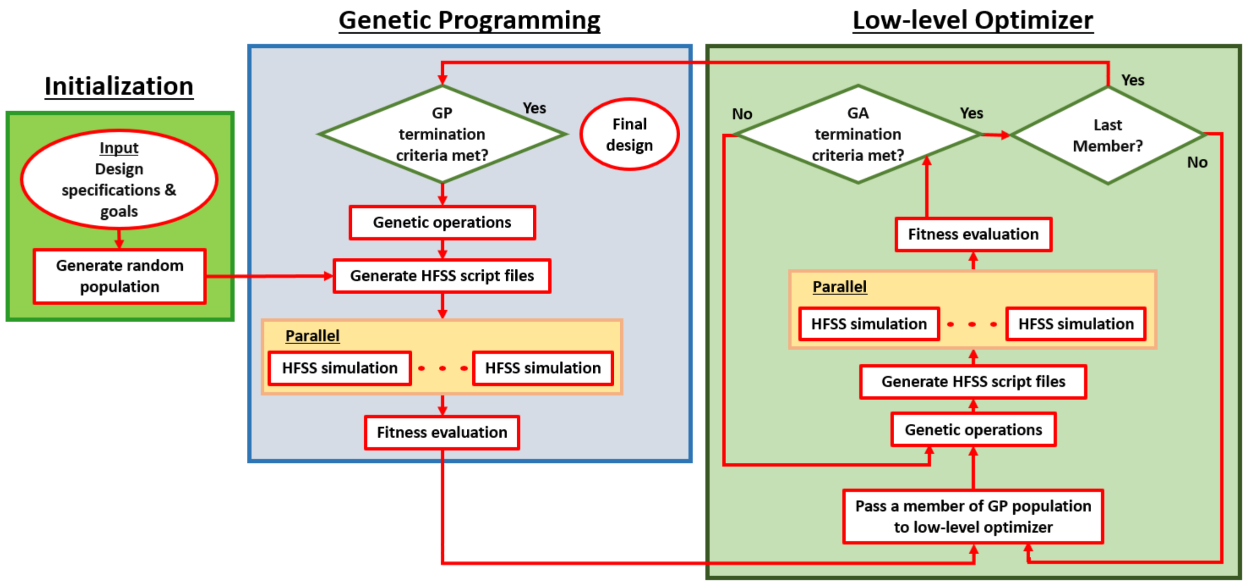

Figure 3.2: HGP flow chart

3.2 Metamaterial Absorber Design Examples

Previously GP was designed for AMCs; by modifying the pattern tree structure and fitness function, the GP for AMCs can create new topologies for absorbers. One characteristic of GP topology optimization is that patterns are not restricted to a single unit cell. Patterns can span neighboring cells and create multiple patterns within an array of unit cells. Applying symmetry within the unit cell removes the aspect of cross-polarization with the design. A modified fitness function that includes the S_{21} parameter from the floquet port also mitigates designs with cross-polarization. GP aims to create new topologies that outperform those designs published in the literature. The following sections provide examples of designs created by GP. These designs are based on the metalization on top of substrates backed by a metallic backplane. Section 3.2.1 presents the initial efforts in using GP with a single-layer dielectric design. Sections 3.2.2 and Section 3.2.3 present two methods to approach broadband characteristics in the lower frequency range, 2D patterning with multilayer substrates and 3D patterning with multilayer substrates.

3.2.1 2D Pattern with Single-Layer Substrate

HGP was used to create new topologies for single-layer substrate designs. The goal was to create new resonant frequencies that are lower in frequency and broader in peaks. A thin substrate of dielectric material similar to FR4 with metallic patterns on top and backed by a metallic backplane was optimized through GP. The design input parameters for the unit cell and substrate are given in table 3.1. Figure 3.3(a) shows the design created by GP modeled in HFSS. The design height is 1.67 mm, and the length and width are 21.4 mm. The design dielectric properties are $\epsilon_r = 4.665$, and the loss tangent tan $\delta_e = 0.0047$. Figure 3.3(b) shows that GP achieved multiple resonant peaks slightly lower in frequency at 5.29 and 7.97 GHz but narrower than the radar-absorbing layer [3] and lower in absorptivity at 0.76 and 0.82 respectively. The design created from GP also created additional resonant frequencies at 10.7 and 11.5 GHz. The lower and additional resonant frequencies demonstrate that HGP can be used to create designs that could converge to broadband designs.

Table 3.1: Design Input Parameter for 2D Pattern with Single-Layer Substrate

Unit cell	x, y = 0.1 - 25 mm, z = 0.4 - 5 mm
Substrate	ϵ_r = 3 - 5, tan δ_e = 0 - 0.005

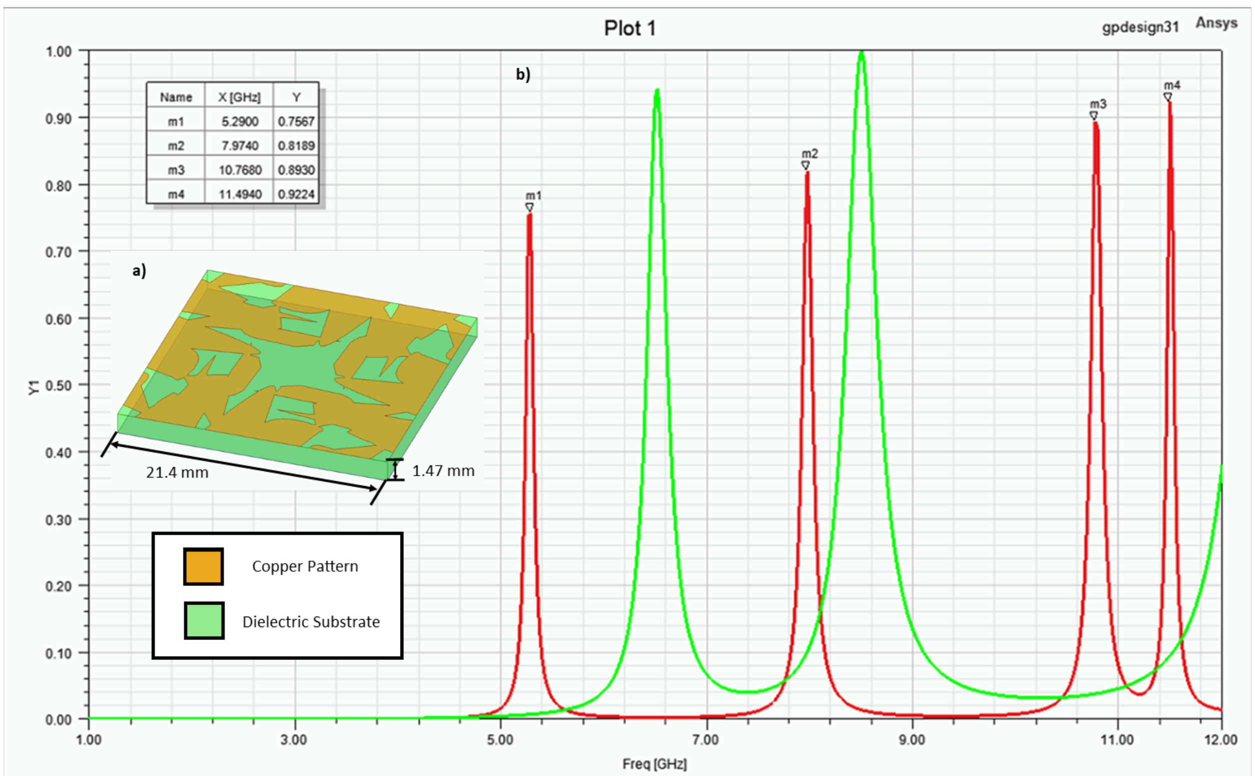

Figure 3.3: (a) 2D Pattern with single-layer substrate design and (b) lower frequency absorptivity peaks compared to RAL design [3]

3.2.2 2D Pattern with Multilayer Substrate

HGP was used to create a 2D pattern on top of multilayer substrates using the same pattern topology as the single-layer substrate design. The goal is to employ HGP to create additional resonant frequencies so that broadband absorptivity can be achieved by coupling multiple resonant frequencies. The substrate tree determines the number of layers of substrates, and each substrate layer in the multilayer stack is individually assigned dimensions and dielectric properties. The design input design parameters for the unit cell and substrate are given in table 3.1. Figure 3.4 shows the multilayer design optimized from GP. It consists of a metallic pattern on top, and three substrate layers, backed with a metallic backplane. The design parameters are t_1 = 8.39 mm, t_2 = 13.95 mm, t_3 = 4.33 mm, $\epsilon_{r1} = 5.28$, $\epsilon_{r2} = 10.96$, $\epsilon_{r3} = 4.99$, tan $\delta_{e1} = 0.0042$, tan $\delta_{e2} = 0.0036$, and tan $\delta_{e3} = 0.0043$. The total height of the design is 26.67 mm, which is 0.1778λ at 2 GHz and the periodicity, p, is 4.05 mm.

Table 3.2: Design Input Parameter for 2D Pattern with Multilayer Substrate

Unit cell	x, y = 0.1 - 25 mm, z = 0.5 - 37.5 mm
Substrate	ϵ_r = 2 - 10, tanδ_e = 0 - 0.005

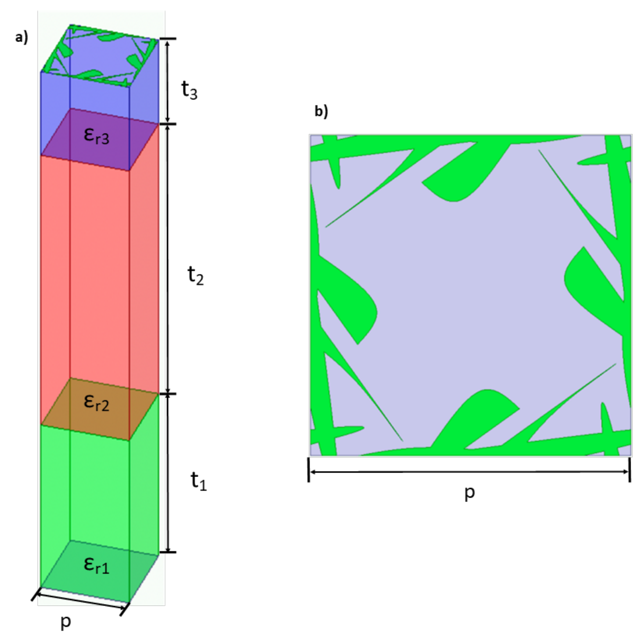

Figure 3.4: (a) 2D pattern with multilayer substrate design and (b) top view of unit cell

Figure 3.5 shows the results of the design in figure 3.4. With this design, there are multiple narrow absorptivity peaks. Table 3.3 lists the frequency and amount of absorptivity, respectively. There are two peaks above 80% at 5.9 and 7.82 GHz, at 0.92 and 0.84 absorptivity, respectively. GP was employed to create 2D patterns with multilayer substrates designs, but the results from this iteration created designs with multiple narrow peaks similar to those of literature designs.

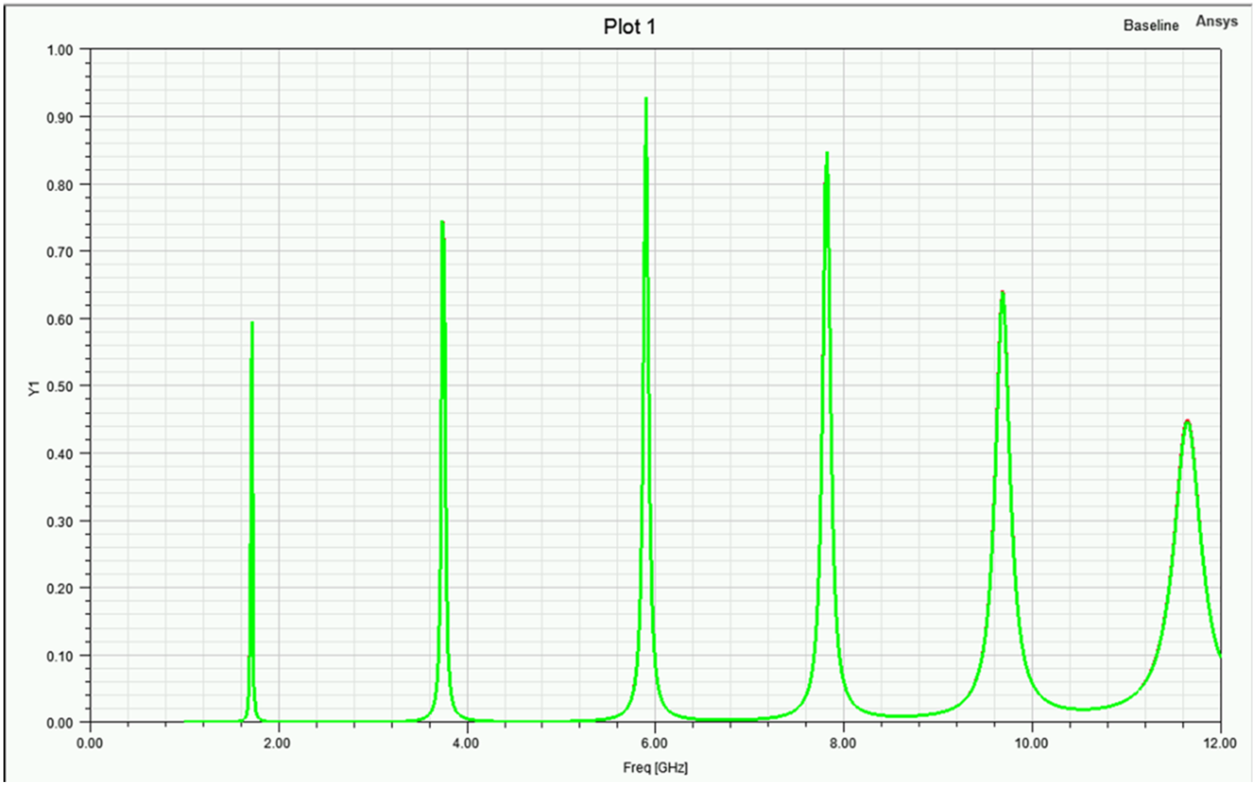

Figure 3.5: Multiple absorptivity peaks from 2D pattern with multilayer substrate design

Table 3.3: Results for 2D Pattern with Multilayer Substrate

Frequency (GHz)	Absorptivity
1.72	0.59
3.74	0.74
5.9	0.92
7.82	0.84
9.68	0.63
11.66	0.44

3.2.3 3D Pattern with Multilayer Substrate

Another method to achieve broadband MMA is using 3D metallic planar wire patterns embedded throughout the substrates. Previously this 3D topology was used to provide increased broadband performance to AMCs [1]. The 3D metallic planar wire patterns can span multiple unit cells, but the wires are wrapped to retain the wire in the unit cell, and the wrapping of the pattern provides a unique wire pattern. Symmetry is applied to the metallic planar wire pattern as well to account for cross-polarization that may occur. The substrate and unit cell generation is the same as the 2D topology design, and the design input parameters are the same as table 3.2. Figure 3.6 shows the 3D topology design with multilayer substrates with the connecting wires across neighboring unit cells shown in the 3x3 unit cell. The design parameters are $t_1 = 14.95$ mm, $t_2 = 5.33$ mm, $\epsilon_{r1} = 8.26$, $\epsilon_{r2} = 2.12$, tan $\delta_{e1} = 0.0031$, and tan $\delta_{e2} = 0.0022$. The total thickness of the design is 20.28 mm, which is 0.1352λ at 2 GHz, and the periodicity, p, is 3.06 mm.

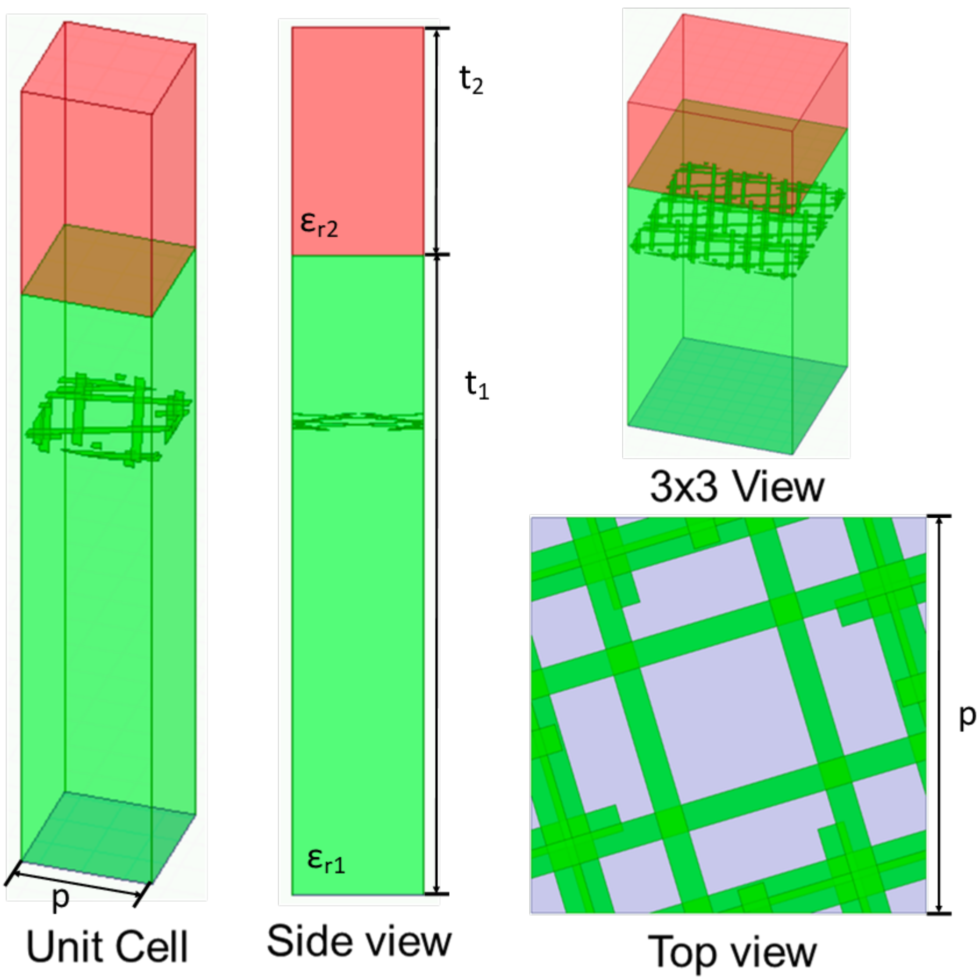

Figure 3.6: 3D pattern with multilayer substrate design

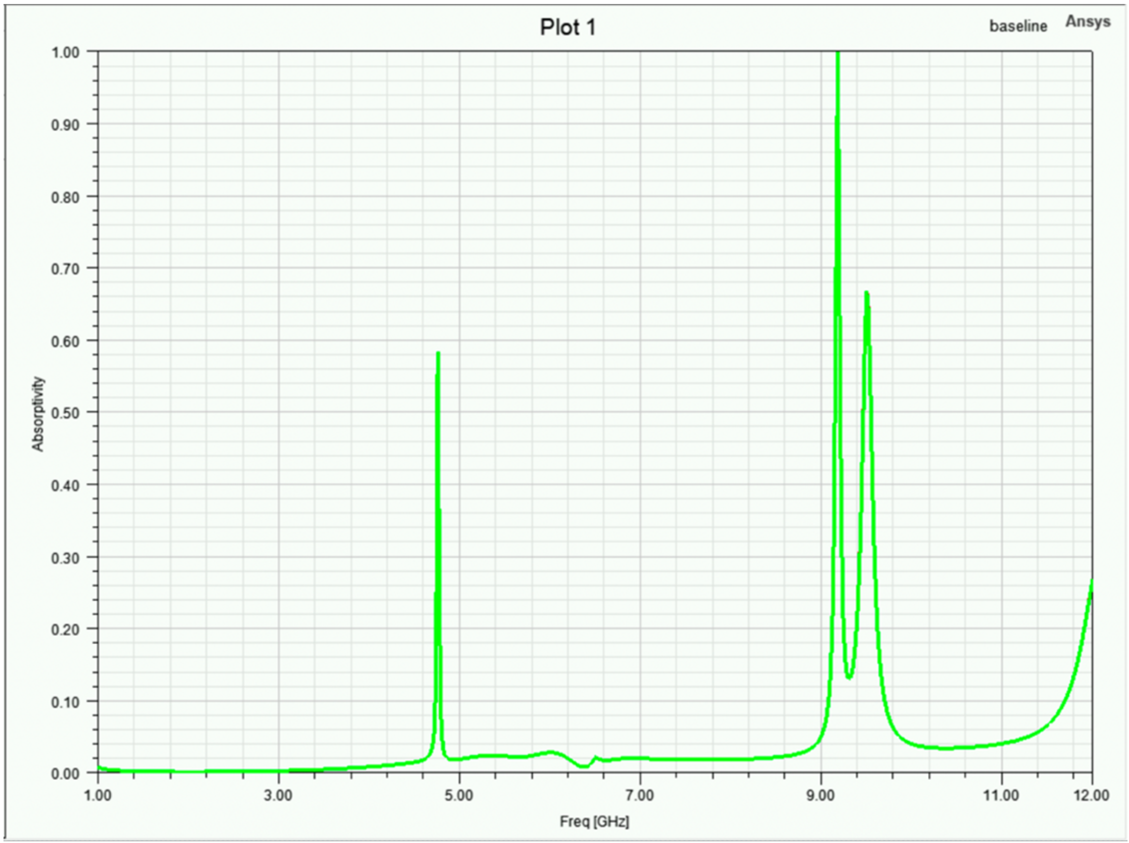

Figure 3.7: Discrete absorptivity peaks for 3D pattern with multilayer substrate, above 80% at 9.18 GHz

Figure 3.7 shows the results of the design in figure 3.6. There is one peak above 80% absorptivity at 9.18 GHz with additional resonant frequencies at 4.76 and 9.5 GHz. Similar to the 2D design, these multiple peaks could couple together and form broadband absorptivity. However, as the initial run with this 3D topology, this design of multiple resonances does not display broadband performance.

HGP was successfully implemented in designing MMAs but did not provide broadband designs with 2D or 3D topologies and multilayer substrates. Although not broadband, GP did produce designs with multiple resonant frequencies, and these designs using metal-based patterning are limited to narrow bandwidths. Applying different materials to be patterned could provide broadband performance.

CHAPTER 4
GRAPHENE BASED DESIGNS

4.1 Graphene

Graphene is a mono-layer of carbon atoms, greatly sought after for its excellent electrical properties and conductivity tunability by an electric field bias. Graphene is most commonly produced by chemical vapor deposition, where gas molecules are deposited onto a substrate. This method uses high temperatures and expels volatile gasses as a by-product. Other methods of creating graphene are through chemical or micromachine exfoliation, where individual graphene layers are taken off of a block of graphite. The graphene produced by exfoliation is small in feature size, and unsuitable for large-scale production [25] [16].

Graphene production is one of the considerable challenges with using graphene as a patterned material, and the other challenge is patterning the graphene itself. The most commonly used method to pattern graphene is the top-down approach of photolithography, and there are numerous methods of implementing photolithography. With challenges at large-scale graphene production, these photolithographic methods end up driving up the cost of production [26].

Laser-induced graphene (LIG) is graphene created by scribing a carbonated polymer with a CO_2 laser. This method of producing graphene is greatly sought after for its ability to create and pattern graphene precisely. This method of producing graphene does not require high-temperature chambers or toxic chemicals. The graphene created by this method is multilayer 3D porous graphene that can be patterned at high precision. The properties of LIG depend on the laser parameters used to create the graphene, such as laser pulse width, laser speed, and energy use. LIG offers a cheaper and more effective way of creating and patterning graphene [27][28]. The advantage of using LIG is that it can fabricate patterned designs, but it has challenges. The challenges include variations in the fabrication process and the impact of nonuniform material properties and how it would affect the MMA's design, the complex permittivity characterization of the multilayer graphene, and determining the graphene conductivity vs. an external electric field bias.

4.1.1 Graphene Characterization

The conductivity of graphene is investigated to gain a better understanding of the conductivity tunability of graphene. Using the Kubo model, the complex surface conductivity can be calculated using intra-band contributions [29]. The complex surface conductivity is

$$\sigma_s = \frac{\sigma_0}{1 + j\omega\tau} \tag{4.1}$$

and

$$\sigma_0 = \frac{q_e^2 k_B T \tau}{\pi \hbar} \{ \frac{\mu_c}{k_b T} + 2 \ln(e^{\frac{-\mu_c}{k_B T}} + 1) \} \tag{4.2}$$

where q_e is the electron charge, k_B is is Boltzmann's constant, T is the temperature, τ is the electro-phonon relaxation time, $\hbar$ is the reduced Plank's constant, μ_c is the chemical potential, and ω is the operation frequency. In microwave frequencies, graphene is frequency-independent [30]. From equation 4.2, the conductivity of the graphene depends on μ_c, the chemical potential. An electric field bias, E_{dc}, can change the chemical potential. The relation between μ_c and E_{dc} is

$$\frac{2\epsilon_0 \epsilon_r E_{dc}}{q_e} = \frac{2}{\pi \hbar^2 v_F^2} \int_0^\infty \mathcal{E}[F(\mathcal{E}) - F(\mathcal{E} + 2\mu_c)] d\mathcal{E} \tag{4.3}$$

and

$$F(\mathcal{E}) = \frac{1}{1 + e^{\frac{\mathcal{E} - \mu_c}{k_B T}}} \tag{4.4}$$

is the Fermi-Dirac distribution, where ϵ_r is the relative permittivity of the substrate the graphene is created with, and v_F is the Fermi speed of graphene. Solving equation 4.3 analytically with equation 4.4. Figure 4.1 shows the relationship between μ_c and E_{dc}. It should be noted that E_{dc} can generally withstand up to 5 V/nm [31].

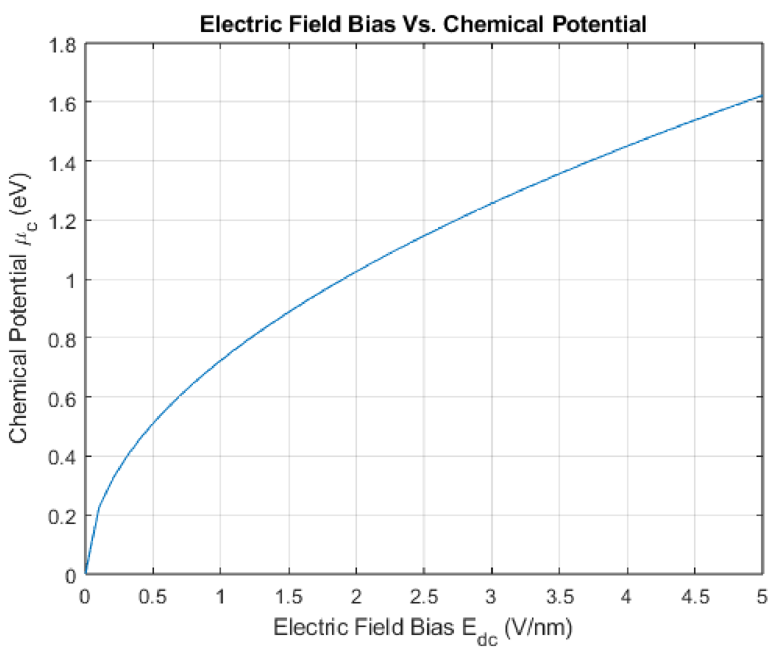

Figure 4.1: Relationship between Electric Field Bias and Chemical Potential

The volume conductivity of graphene can be estimated by dividing the complex surface conductivity's magnitude by the graphene's thickness.

$$\sigma = \frac{\sigma_s}{t_{graphene}} \tag{4.5}$$

A function incorporating equations 4.1-4.5 was created in MATLAB, listed in Appendix A. Given the substrate's permittivity, the graphene's thickness, operational frequency, electric field bias, and electron-phonon relaxation time, the function returns the conductivity of graphene. The parameters used to calculate the graphene's conductivity are as follows, the substrate used for LIG is polyimide, $\epsilon_r = 3.5$, the graphene thickness, $t_{graphene} = 31\mu$m, operational frequency, $f = 2$GHz, the electro-phonon relaxation time, $\tau = 1$ps (for low impurity graphene for better absorption) [31]. Three values of electric field bias were chosen to represent no bias, low bias, and high bias at $E_{dc} =$ 0, 0.5, and 4 V/nm, respectively. Table 4.1 shows the corresponding graphene conductivities to the electric field bias.

Table 4.1: Graphene Conductivity at Different Electric Field Biases

Electric Field Bias, E_{dc} (V/nm)	Conductivity (S/m)
0	27.2
0.5	387.9
4	1101.2

4.2 Graphene Pattern Designs

HGP was used to create three new designs at the three different conductivities. The 2D topology with a single-layer substrate was used to create these designs. Previously with the metallic pattern designs, the pattern geometry created by GP was assigned as a PEC in HFSS. With the new graphene conductivity values, the geometry is assigned as Finite Conductivity in HFSS. The substrate is set to polyimide, $\epsilon_3.5$, and loss tangent, $\tan\,\delta_e = 0.0026$. The unit cell dimensions were set to X, Y = 0.1-25 mm, and height, t = 0.5-10 mm. Figure 4.2 shows the unit cells of each design, and each design is optimized to its respective conductivity value. Table 4.2 lists the substrate dimensions of each design.

Table 4.2: Unit Cell Dimensions for Graphene Based Designs

Design	Unit cell XY, p (mm)	Unit cell height, t (mm)	Unit cell height, t (λ at 4GHz)
0 V/nm	6.65	5.17	0.069
0.5 V/nm	4.15	3.94	0.0525
4 V/nm	6.65	1.63	0.0217

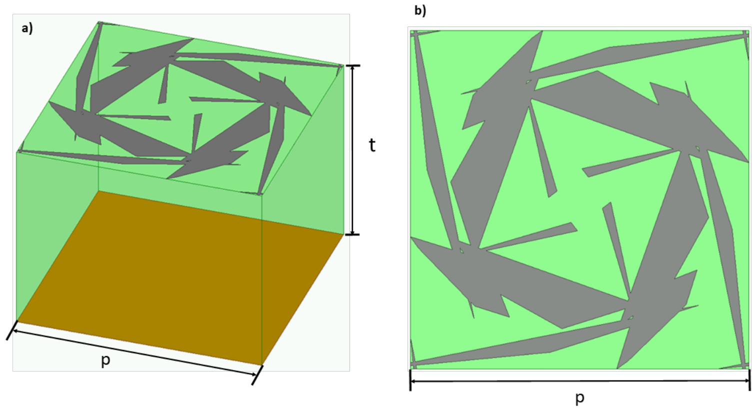

(a) E_{dc} = 0 V/nm, σ = 27.2 S/m, side view (left), top view (right)

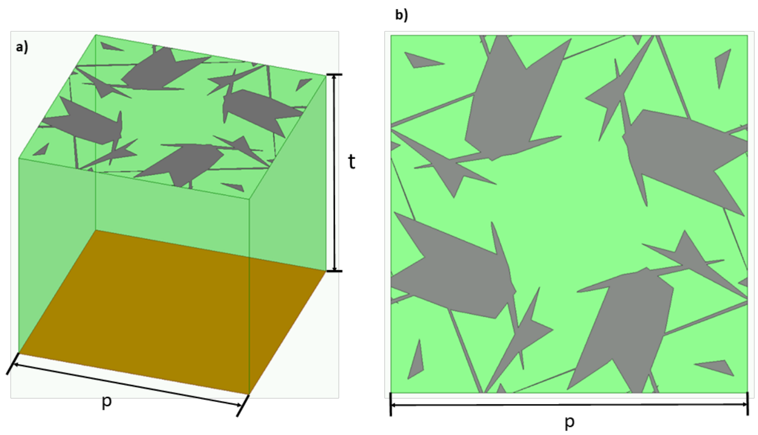

(b) E_{dc} = 0.5 V/nm, σ = 387.9 S/m, side view (left), top view (right)

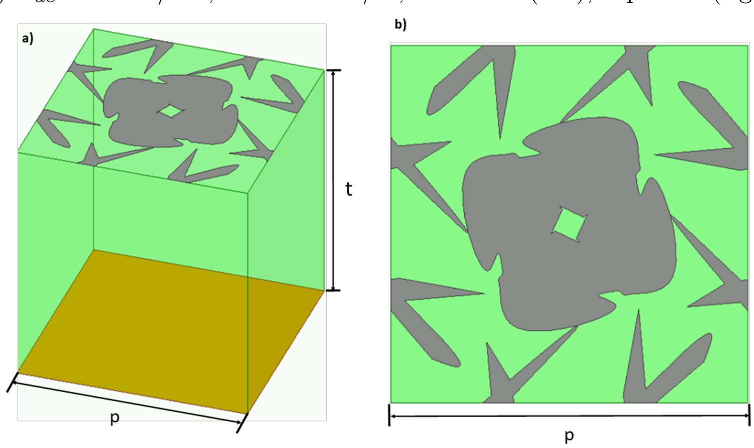

(c) E_{dc} = 4 V/nm, σ = 1101.2 S/m, side view (left), top view (right)

Figure 4.2: Graphene based pattern designs, (a) 0 V/nm bias, (b) 0.5 V/nm bias, (c) 4 V/nm bias

Figure 4.3 shows the absorptivity performance for all three designs—each design achieved above 80% absorptivity and above 80% bandwidth. Table 4.3 lists the frequency range where the designs achieve broadband performance. HGP was able to create broadband-performing designs at three different graphene conductivities. As the graphene conductivity increases, the bandwidth of the absorptivity increase as well. Graphene, as a patterned material, achieved broadband performance with the designs created by HGP. With LIG, precisely patterned graphene-based absorbers can be realized. Although the designs provided achieve broadband performance in simulation, the simulations do not consider the nonuniformities that may occur during the production of LIG.

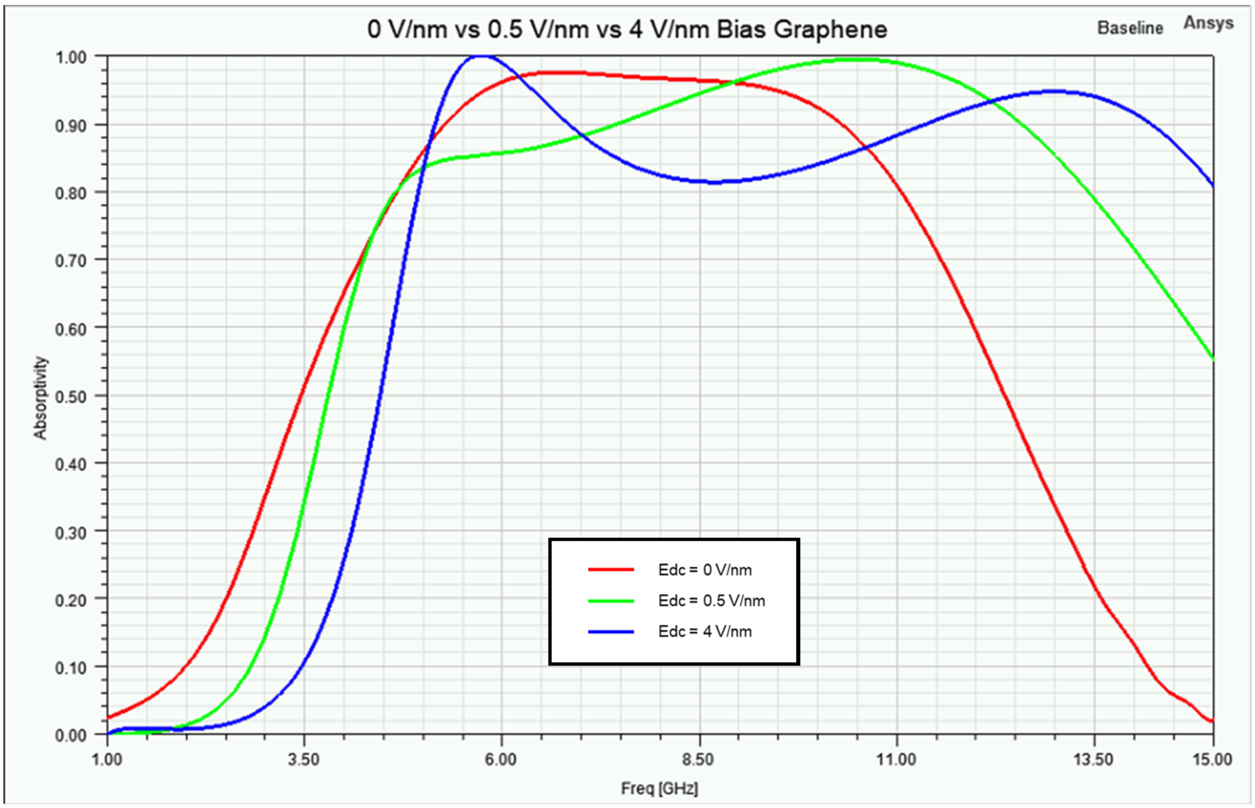

Figure 4.3: Broadband absorptivity above 80% for all three graphene based designs

Table 4.3: Performance of Graphene Based Designs Above 80% Absorptivity

Design	f_{min} (GHz)	f_{max} (GHz)	Bandwidth
0 V/nm	4.6	11	82.05%
0.5 V/nm	4.6	13.39	97.72%
4 V/nm	4.94	15	100.9%

4.3 Nonuniformity

The nonuniformities during the production of LIG depend on the tolerances of the laser used to scribe the carbonated polymer [28]. Nonuniformities can form from the difference in conductivity during the scribing process. As the laser passes across the substrate, nonuniformities in conductivity can occur from path to path. Another source of nonuniformity comes from the overlap of graphene, creating multilayered graphene that could have different conductivity. Sections 4.3.1 and 4.3.2 will investigate the effects of these nonuniformities on the laser track and the multilayered graphene, respectively.

4.3.1 Laser Track Width

The laser track is spaced 100 μm apart to simulate the nonuniformities within the laser track width. The design used for simulating nonuniformities is the 0.5 V/nm bias design where the conductivity, $\sigma = 387.9$ S/m. Two circumstances are considered where the laser track has a width of 10 μm and 50 μm. The strips were denoted at a quarter of the conductivity, $\sigma = 96.98$ S/m, half of the conductivity, $\sigma = 193.95$ S/m, and no graphene for each case. Figure 4.4 shows a quadrant of the 0.5 V/nm design and how the laser track is simulated where the black strips are the nonuniformities at quarter conductivity, half conductivity, or no graphene.

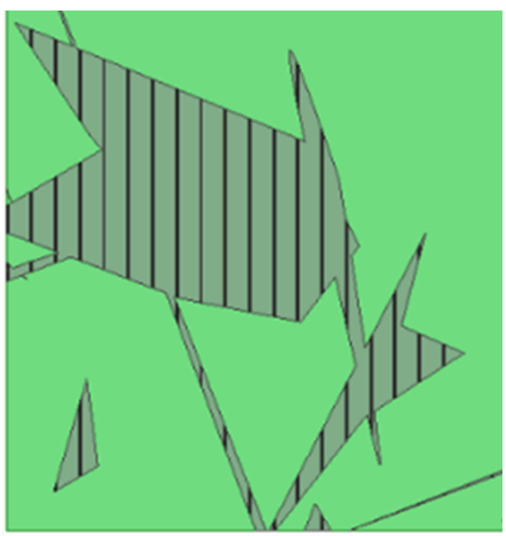

(a) 10 μm width strips

(b) 50 μm width strips

Figure 4.4: 0.5 V/nm design, $\sigma = 387.9$ S/m, the black strips represent quarter conductivity, half conductive, or no graphene (a) 10 μm width strips, (b) 50 μm width strips

Figure 4.5 shows the absorptivity of the different nonuniformity cases at 10 μm and 50 μm. The band structure with 10 μm and 50 μm strips at a quarter and half conductivity has an average bandwidth of 66% at above 80% absorptivity from 6.3 to 12.4 GHz. The bandwidth for the 0.5

V/nm design is 97.72%; the nonuniformities reduce the bandwidth by about 32%. The absorptivity drops drastically as the gap width increase. Removing graphene at the same width at 10 μm and 50 μm destroyed the broadband performance above 80% absorptivity. Nonuniformity in graphene fabrication tends to have a limited impact on the performance of the designed metamaterials.

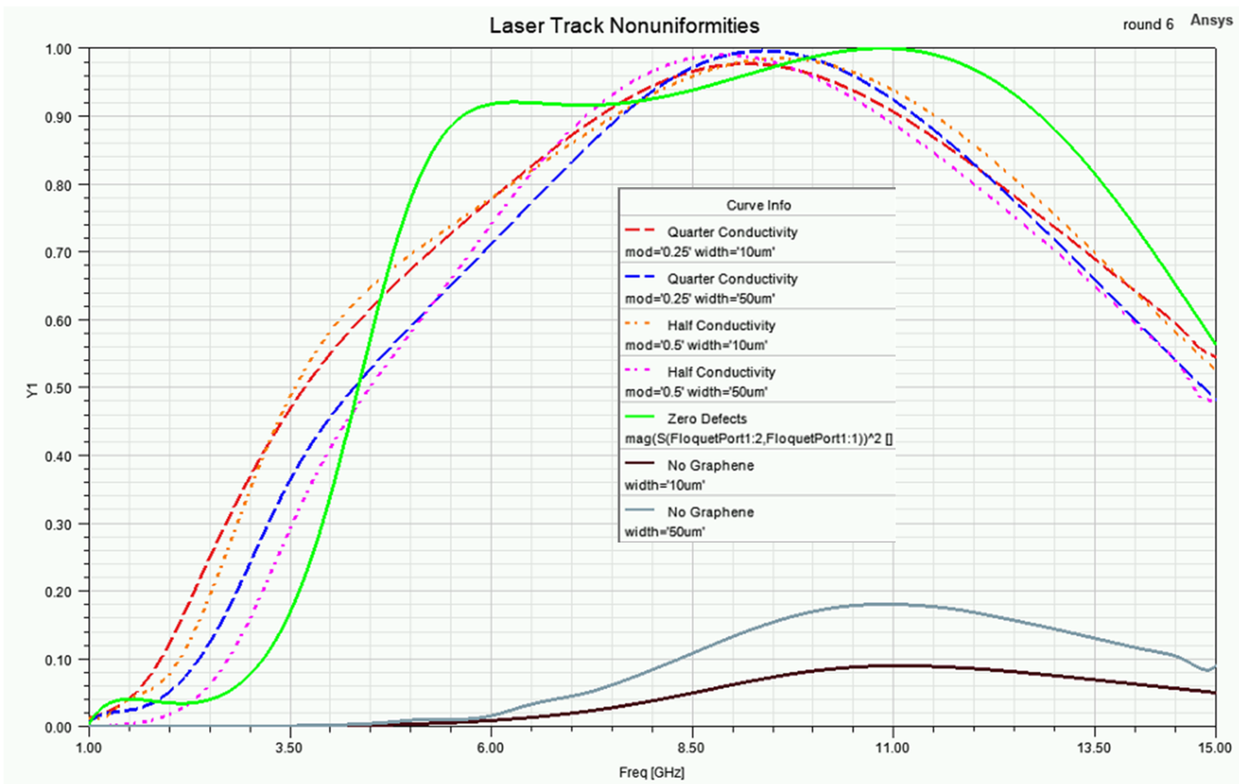

Figure 4.5: Absorptivity of laser track width nonuniformities at quarter conductivity, half conductivity, or no graphene

4.3.2 Multilayer Graphene

When a design is created from HGP and simulated in HFSS, the top pattern is created as a sheet element with no thickness. The pattern needs to be thickened before simulating the nonuniformity of multilayered graphene. The thickness of graphene used in conductivity calculations is 31 μm. When a sheet element is thickened in HFSS, the edges of the pattern that intersect with the airbox connecting to neighboring cells cause an error due to overlapping boundaries from the finite conductivity boundary and master and slave pair boundaries for the floquet port. Only the pattern elements not intersecting the airbox will be assigned a finite conductivity boundary not to have overlapping boundaries. Patterns self-contained in the unit cell do not have this issue because there are no overlapping boundaries. Figure 4.6(a) shows the 31 μm layer of graphene for the 0.5 V/nm bias design, and figure 4.6(b) shows the 31 μm layer of graphene but the top half of the graphene is half the conductivity at σ = 193.95 S/m, and the bottom half is the total conductivity at σ = 387.9 S/m.

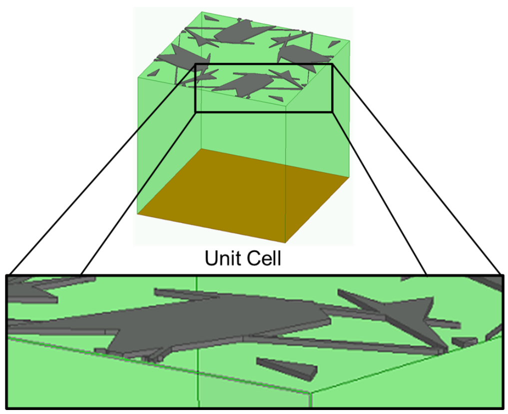

(a) 31 μm thick layer of graphene

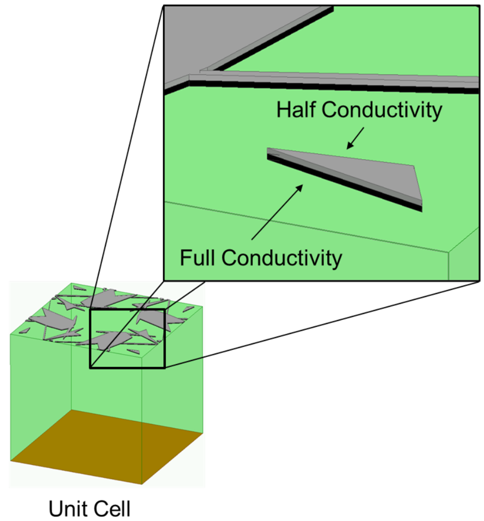

(b) 31 μm thick layer of graphene, top half is half the conductivity and bottom half is full conductivity

Figure 4.6: 0.5 V/nm design, σ = 387.9 S/m, (a) 31 μm thick layer of graphene at full conductivity, (b) half conductivity on top of full conductivity

Figure 4.7 shows the absorptivity of the 31 μm thickness model, 31 μm thickness 50:50 model, and the original 0.5 V/nm bias design. There are minor differences in the band structure between the two thickened models. The significant difference was the drop in performance when the pattern went from a sheet element to a volume element. The bandwidth of the thicken model is about 47% above 80% absorptivity from 5.7 to 12.45 GHz. The difference between the original design and the thicken model is about 50% in bandwidth reduction. Multilayering in LIG fabrication tends to impact the achievable broadband characteristics of designed MMAs considerably.

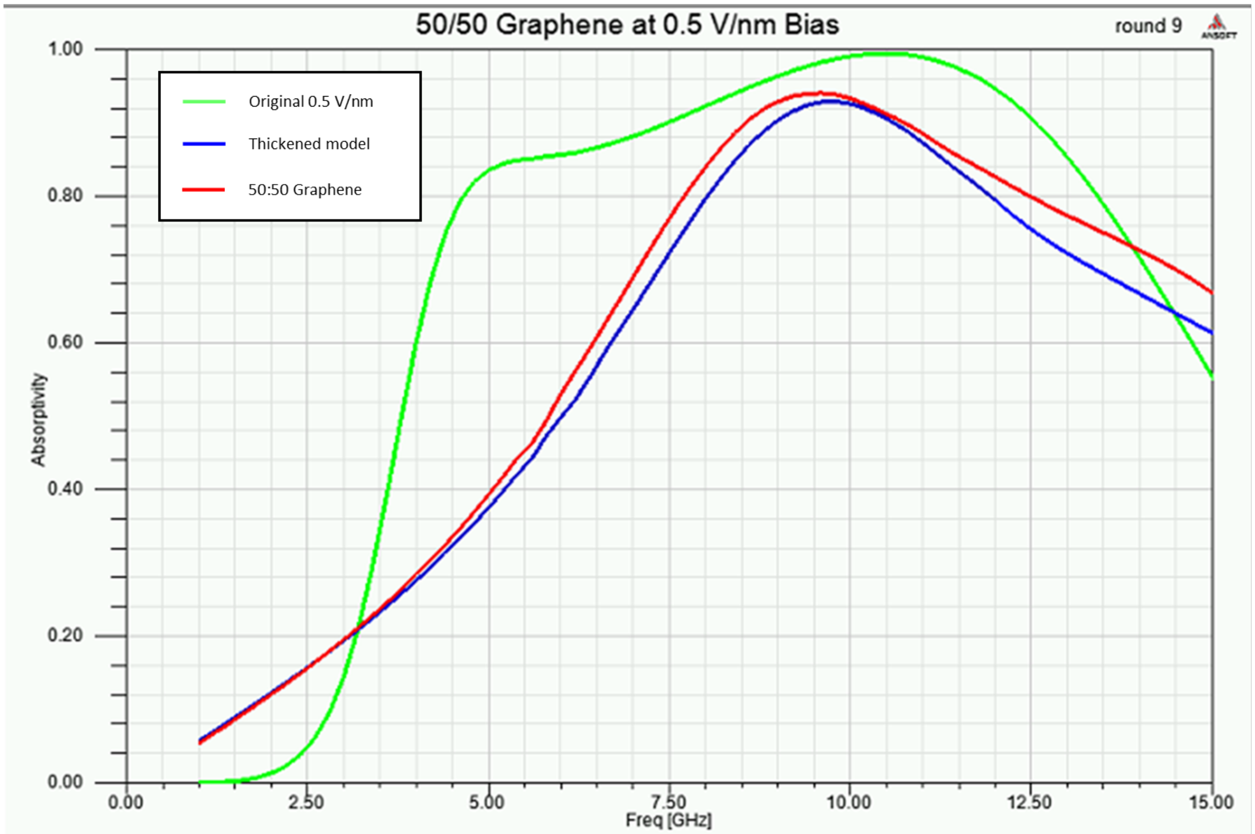

Figure 4.7: Thicken modeled results vs original 0.5 V/nm

4.4 Pattern Round Off

The designs created by HGP can have features smaller than the laser spot size used in LIG fabrication. In the 0 V/nm bias design, the pattern has several small and sharp features. Figure 4.8(a) highlights some of these features in a quadrant of the 0 V/nm design. The design has four-fold symmetry, so any changes made in one quadrant can be equally applied to the entire unit cell. Figure 4.8(b) is the modified pattern after removing small and sharp features. The modifications are removing the connecting segment with neighboring cells, removing and rounding off sharp angles, and filling tiny holes in the pattern.

Figure 4.9 shows the absorptivity of the 0 V/nm bias design and the modified model. Even with certain features removed, the overall band structure is relatively the same as the original design. Rounding off the edges of the designs demonstrates that the broadband performance is persistent even if the pattern has to be modified to account for the laser spot size.

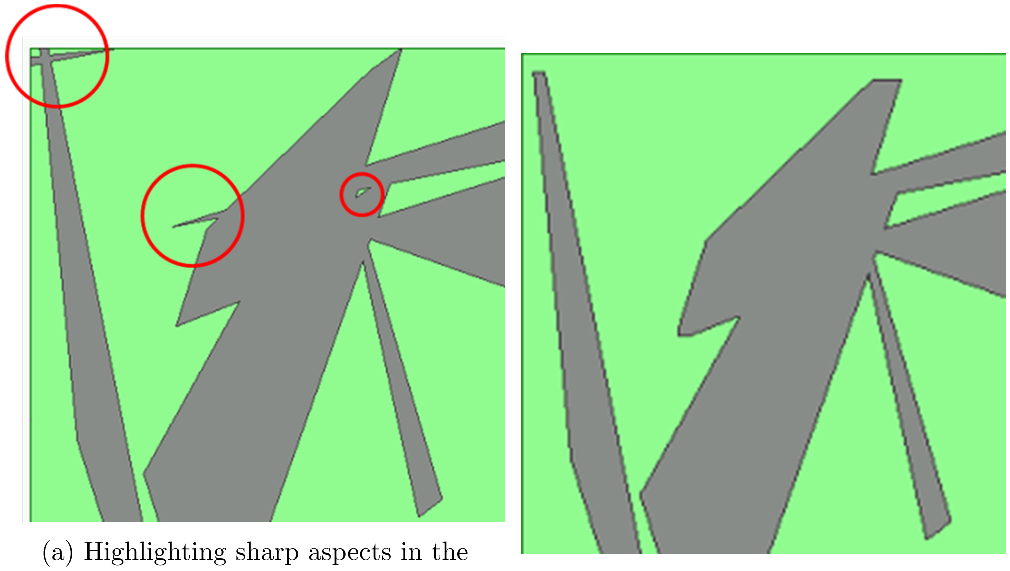

(a) Highlighting sharp aspects in the pattern in the top left quadrant of 0 V/nm design

(b) Top left quadrant of 0 V/nm design with sharp aspects removed

Figure 4.8: Top left quadrant of 0 V/nm design, (a) original design, (b) rounded off edges

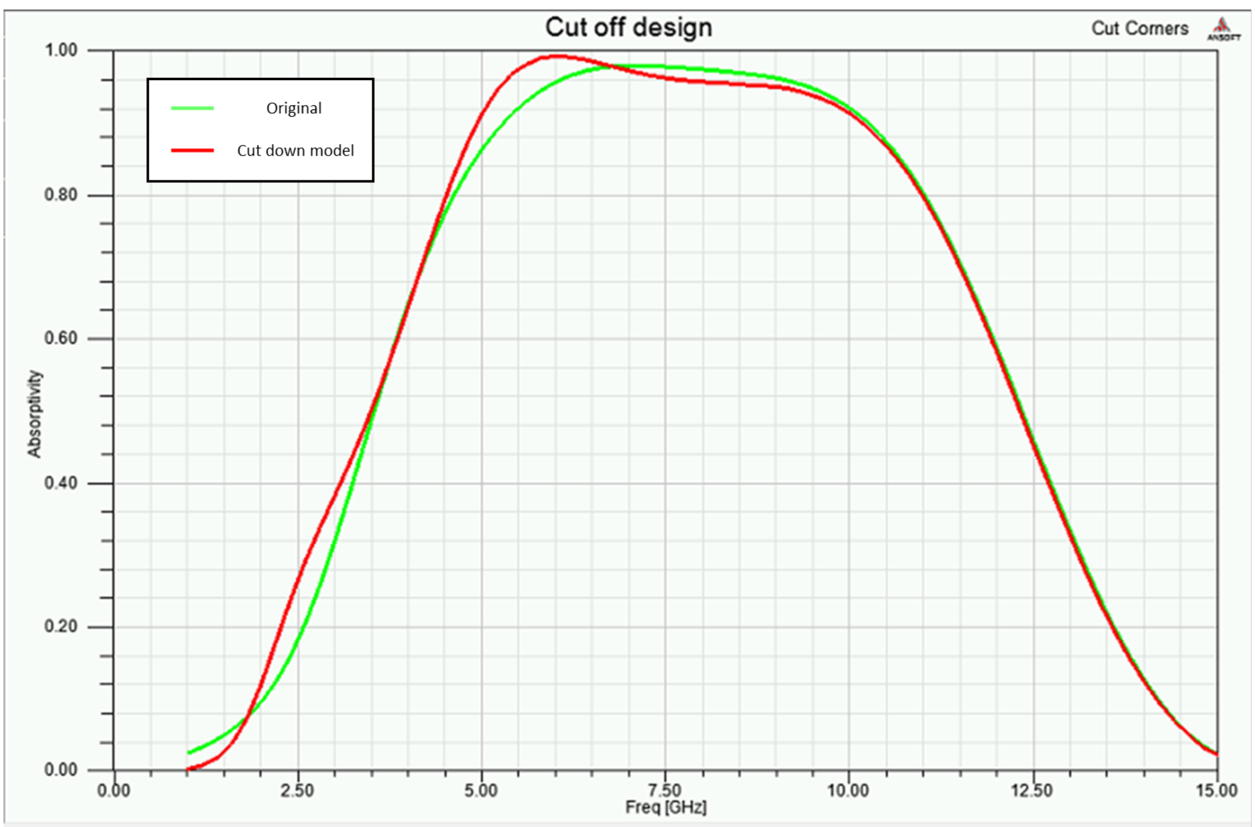

Figure 4.9: Absorptivity of 0 V/nm design and modified model

CHAPTER 5
RESISTIVE SHEET BASED DESIGNS

5.1 Resistive Sheets

Resistive sheets have been used in the past to create broadband MMAs. The approach to using resistive sheets is based on impedance matching with the characteristic impedance of free space. By matching the impedance of free space, the reflection coefficient is at a minimum, yielding high absorption [4][15][32].

HGP can be implemented with resistive sheets to create new topologies that provide broadband performance. Compared to graphene, resistive sheets have been established for commercial use. Resistive sheets might not be as tunable as graphene, but resistive sheets come in various materials and resistances. Existing PCB fabrication techniques, such as milling, can be applied to resistive sheets to provide cheap, fast, and precise patterning.

5.2 Resistive Sheet Pattern

HGP was implemented using a resistive sheet as a patterned material. Similar to the graphene implementation with HGP, the 2D topology with a single-layer substrate is used, and the pattern element is assigned as an impedance boundary instead of PEC. The substrate used is close to FR4, $\epsilon_{=}$ 3-4, with loss tangent, tan δ_e = 0-0.005. The unit cell dimensions were set to X, Y = 0.1-50 mm, and height, t= 0.5-5 mm. The sheet resistance used for this design was optimized to 100 $\Omega/\Box$ [15]. Figure 5.1 shows the unit cell for the resistive pattern; the properties of the substrate are ϵ_r = 3.9 and tan δ_{e1} = 0.0021. The periodicity of the unit cell, p = 23.37, the height, t = 4.94 mm = 0.0658λ at 4 GHz.

Figure 5.2 shows the absorptivity of the resistive pattern design. The bandwidth of the design is 81.72%, above 80% absorptivity at 3.83 to 9.13 GHz. The performance of this design at 100 $\Omega/\Box$ is comparable to the graphene designs from section 4.2. Comparing figure 5.2 to figure 4.3, the 100 $\Omega/\Box$ design achieved a lower frequency at 80% absorptivity. As an alternative material to graphene, broadband performance was achieved by implementing HGP with resistive sheets.

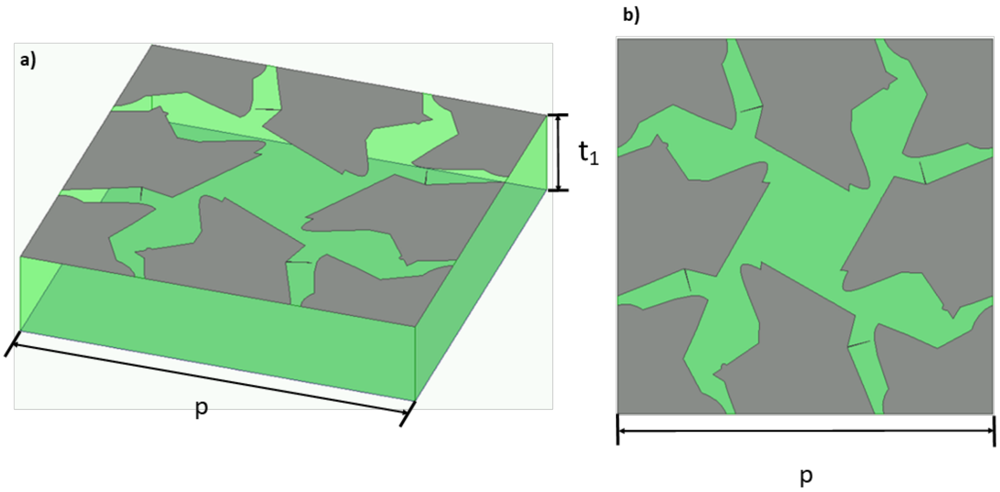

Figure 5.1: 2D resistive pattern with single-layer substrate design, (a) side view, (b) top view

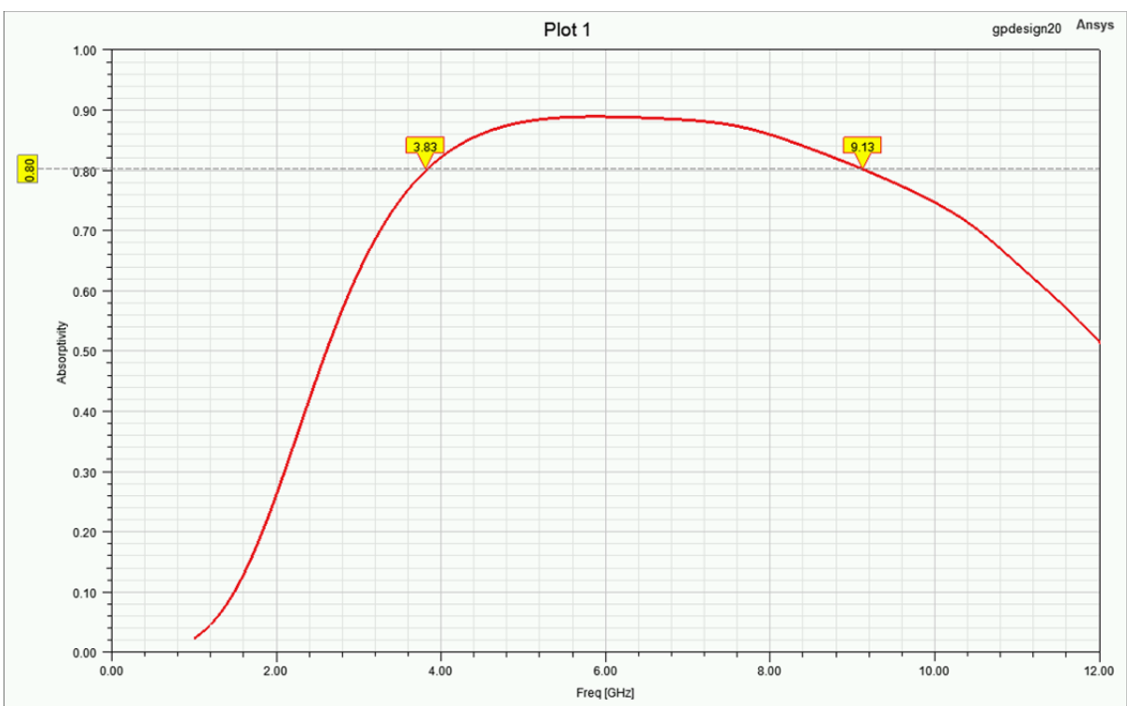

Figure 5.2: Broadband absorptivity above 80% from 3.83 GHz to 9.13 GHz

5.3 Resistive Sheet Insert

Another approach to creating resistive sheet-based designs is inserting a resistive sheet between the substrate for a metallic-based patterned design. In terms of fabrication, adding resistive sheet material between a substrate is trivial. The topology required for this design is a 2D topology with multilayer substrates for creating and simulating a resistive sheet between two substrates. There needs to be a minimum of two substrates, and the area where the two substrates interface is assigned an impedance boundary. Since this is a metallic-based patterning, the pattern created is assigned as PEC again. The design parameters for the substrate are set to FR4, $\epsilon_{=}$ 3-4, and tan δ_e = 0-0.005 so that the metallic pattern can be easily fabricated on top. The unit cell dimensions were set to X, Y = 0.1-50 mm, and height, t= 0.5-5 mm. The design was optimized towards a resistive sheet of 200 $\Omega/\square$. Figure 5.3 shows the resistive sheet insert design—a copper pattern on top of two dielectric substrates, a resistive sheet in between the substrates, and backed by a copper backplate. The properties of the substrate are $\epsilon_{r1} = 3.27$, $\epsilon_{r2} = 3.59$, tan $\delta_{e1} = 0.0043$, and tan $\delta_{e2} = 0.0043$. The unit cell dimensions are p = 30.8 mm, t_1 = 1.74 mm, and t_2 = 1.1 mm. The total height of this design is 2.75 mm or 0.036λ at 4 GHz.

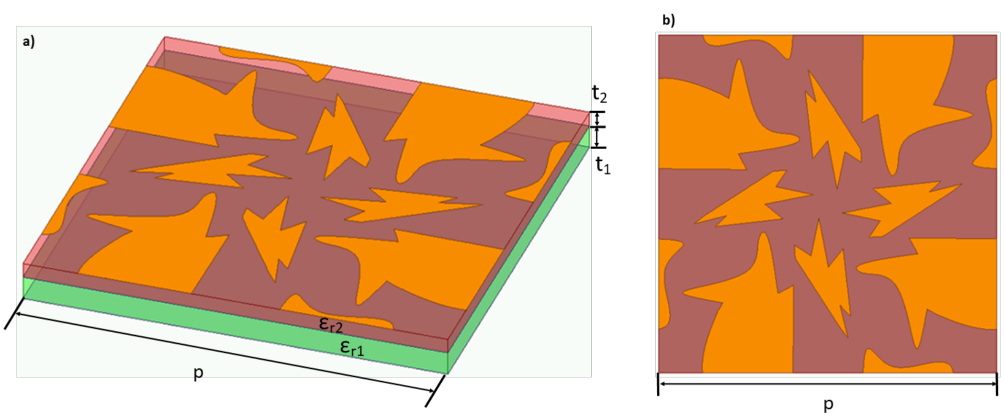

Figure 5.3: 2D copper pattern with single-layer substrate with resistive sheet insert design, (a) side view, (b) top view

Figure 5.4 shows the absorptivity of the resistive sheet insert design compared with the RAL literature design [3]. The resistive sheet insert design achieved above 80% absorption from 4.8 to 6 GHz and 7.1-7.8 GHz. The bandwidth of the peaks is 22.59% and 9.26%, respectively. The resistive sheet insert design outperformed the single substrate literature design regarding broader and lower frequency peaks by optimizing for the resistive sheet and additional substrate layer.

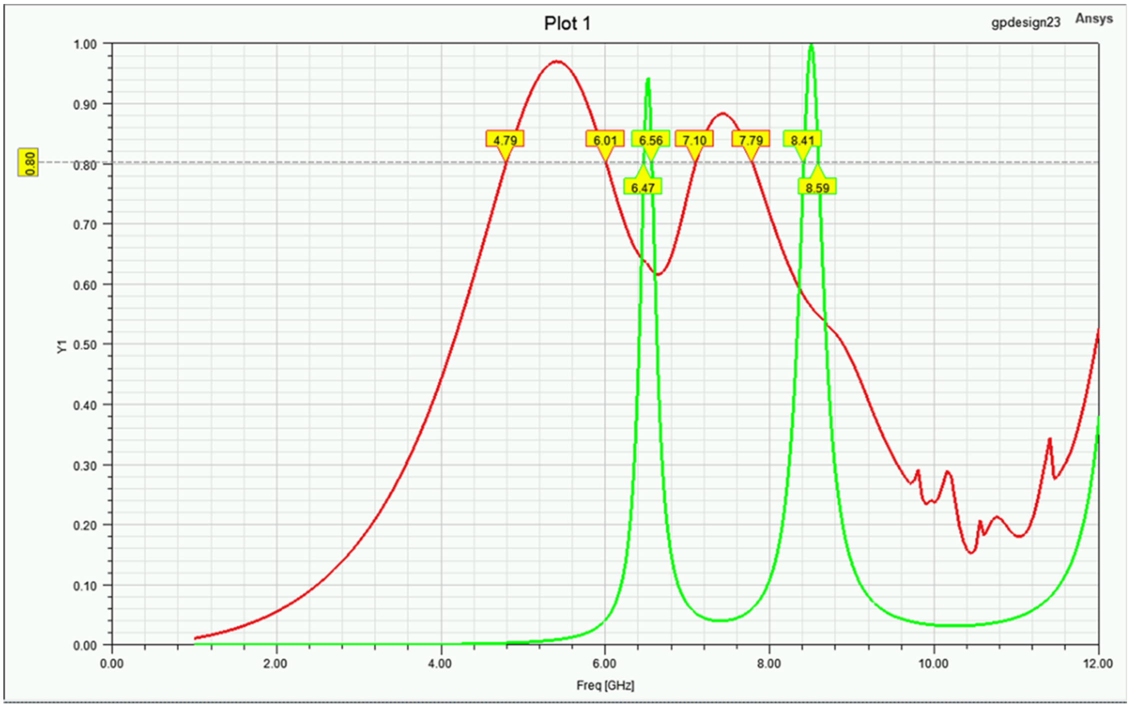

Figure 5.4: Absorptivity above 80% from 4.79 GHz to 6.01 GHz & 7.10 to 7.79 GHz compared with RAL literature design [3]

5.4 Initial Testing and Experimentation Verification

The copper design created by HGP in section 5.2 was fabricated for experimental verification. The center frequency of the lower peak of the resistive sheet insert design is 5.4 GHz, $\lambda = 5.55$ cm. At 10λ x 10λ, the board dimentions is about 55.5 x 55.5 cm^2. The board was fabricated at 18x18 unit cells, with the unit cell length of the resistive sheet insert designs at 30.8 mm. The thickness of the FR4 is about 0.9 mm; the fabrication house used did not have the exact spec of 1.1 mm for the substrate. A carbon-loaded polyethylene plastic film of 200 $\Omega/\square$ is used as the resistive sheet insert. The complete geometry of the designs consisted of the fabricated board with the copper pattern on top of FR4, backed with the carbon-loaded polyethylene film, followed by a 2.3 mm thick sheet of plexiglass, finished with a copper backplane. Figure 5.5 shows the fabricated board in the anechoic chamber for measurements. Two horn antennas were placed incident to the board, and the S parameters were recorded.

The measurement data is processed in MATLAB and plotted against the simulated performance, as shown in figure 5.6. The simulated performance included the original design and the other case where the bottom substrate is adjusted for using plexiglass instead. Comparing the measured data to the original design, the band structure of the first absorption peak is present in the measured data but shifted down. The absorption peaks are better aligned when comparing the measured

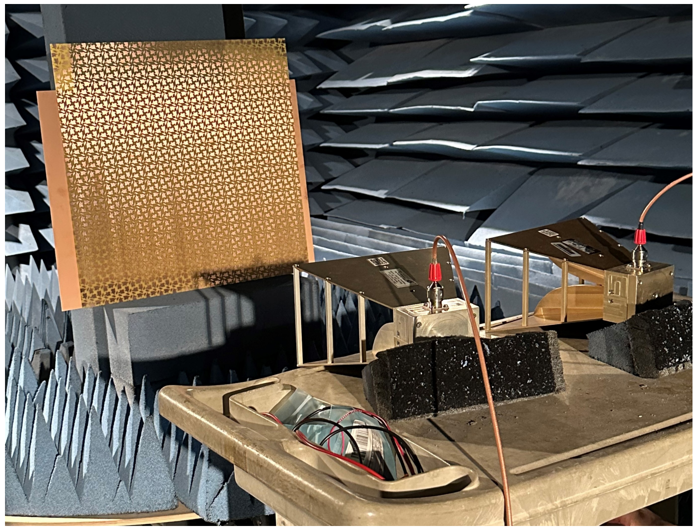

Figure 5.5: Measuring fabricated board in anechoic chamber

data to the data of the simulated design with plexiglass. The fabricated design was successful in matching with simulated results.

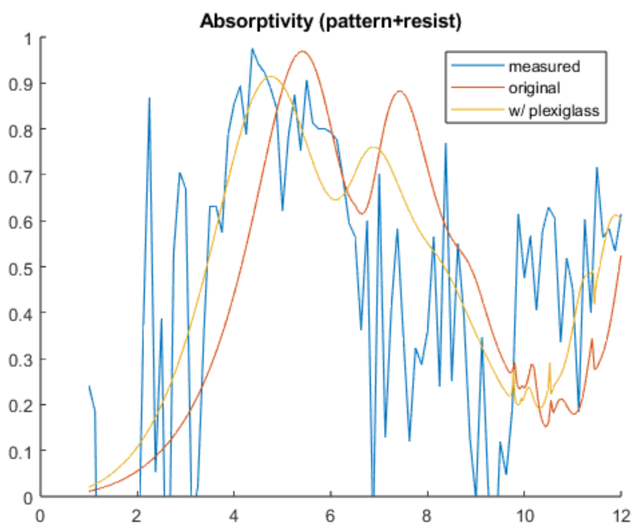

Figure 5.6: Measured absorptivity of fabricated board compared with simulation results

CHAPTER 6
SUMMARY AND CONCLUSION

The research in this thesis aims to explore new material developments with genetic programming to create new MMAs in the low gigahertz frequency with broadband performance. This goal was achieved by implementing graphene-based patterning based on the tunability of the conductivity of graphene, resistive film-based patterning, and resistive sheet insert between the substrate with HGP. HGP, previously used to create 3D metamaterial AMC designs, was modified for MMA by changing the pattern topology and fitness function. Five designs were created with GP to demonstrate achieving this goal. Three graphene-based absorbers from different conductivity designs based on 0, 0.5, and 4 V/nm, one with resistive-based patterning and one with copper pattern and a resistive sheet inserted between the substrate, were designed, and simulated results were presented. The graphene-based and resistive sheet-based patterned designs achieved 80% bandwidth above 80% absorptivity from 4.6 to 11 GHz, up to 15 GHz, and from 3.83 to 9.13 GHz, respectively.

HGP was first used on 2D and 3D metallic topologies with multilayer substrates, but HGP could not provide broadband performance. Graphene was introduced as a substitute material for metal patterns for its conductivity tunability. The patterning of graphene was based on LIG on polyimide, and nonuniformities in the production of LIG on polyimide were examined. Laser track gaps, multilayer graphene, and pattern round-offs do not destroy the band structure of the GP-generated design. Although nonuniformities retain the band structure, LIG requires equipment such as a CO_2 laser to fabricate the patterned design. A resistive sheet insert between the substrate of a metallic patterned-based metamaterial was investigated for its ease of fabrication compared to LIG. Resistive sheets are commercially available for sheet insert or patterning, and resistive material for patterning is significantly more manageable to implement into existing industry fabrication techniques than graphene. Fabrication of the resistive sheet insert design validated that HGP can create optimized designs that provide broadband performance. The measurements of the fabricated board aligned with the simulated results. As material characterization improves, HGP can be unleashed in other frequency regions, such as infrared or optical spectrums.

CHAPTER 7
FUTURE WORKS

Improvements to HGP can be implemented for more robust designs. Evaluating a design's performance at different incident angles allows for creating designs that are incident angle-independent. The incident angle could be implemented by modifying the fitness function. The performance of a design at different incident angles will have to be weighted in the fitness function for HGP to determine that designs with increased incident angle performance be evaluated appropriately.

Another method of improving the designs from HGP is to add graphene conductivity and sheet resistance as a floating variable to be optimized instead of having GP optimize towards a specific value. The flexibility of letting the GP decide what conductivity or sheet resistance values could result in designs that were otherwise not discovered if only restricted.

Another method to approach increased broadband performance is multilayered patterned designs; in the current iteration of HGP, the 2D pattern is restricted to the top of the unit cell. A combination of multilayer substrates and patterns could yield designs with increased broadband performance. The fabrication of this new topology is simple to implement as opposed to a 3D topology with embedded wires throughout the substrate.

A step towards validating the performance of these designs will be to fabricate the proposed graphene and resistive sheet pattern designs and experimentally verify the performance of these designs.

A big challenge with this research has been characterizing graphene and the fabrication process of LIG. The limitations of using graphene as patterned material are as follows. An accurate description of the electrical properties of LIG is still needed, and knowing the complex permittivity of the graphene created allows for an accurate description of LIG in HFSS. The 3D porous nature of LIG makes it challenging to measure the exact properties of graphene, and the Kubo model can only provide a fundamental description of the conductivity. The infrastructure to create and pattern LIG is not commercially available for large-scale production. LIG is still developing, where control over graphene production varies depending on the laser used and different operational modes. As laser parameters are dialed in, LIG's tunability can be endless [33].

Knowing a material's complex permittivity, conductivity, or sheet resistance allows accurate simulations in HFSS, and these properties can be measured. A new method to measure the dielectric properties of thin samples similar to FDTD is being developed. A coaxial probe is still required to take measurements of the reflection magnitude and phase of tested samples, the simulation is done in HFSS, and a GA is implemented to optimize and score the simulated reflection magnitude and phase against a fitness function. The GA iterates the complex permittivity of the thin sample in HFSS until the simulated phase and magnitude are within a pre-determined percent of error.

APPENDIX A
GRAPHENE CONDUCTIVITY FUNCTION CODE

```
function [Conductivity] = graphene(A,B,C,D)
%A = Permittivity
%B = graphene thickness (can be an array of thickness)
%C = frequency
%D = Electric Field Bias

Epsilon_o = 8.8541878176*10^(-12);
qe = 1.60217657*10^(-19);
kB = 1.3806488*10^(-23);
hbar = (6.62606957*10^(-34))/(2*pi);
vF = 10^6;
Tau = 0.2*10^(-12);  %(* low-purity graphene *) % [0.2, 0.34, 1] ps
Temp = 300;
kBT = kB*Temp;
%Permitivity of substrate
Epsilon_r = A;
Epsilon_dchost = Epsilon_r * Epsilon_o;

%Thickness of Graphene layer
dgr_um = B;
dgr_m = dgr_um .*10^-6;

%Frequency
fGHz = C;
freq = fGHz*10^9;
Omega = 2*pi*freq;

%Electric Field Bias
EdcVnm = D; %V/nm
EdcVm = EdcVnm*10^9; %V/m

%%
delta = 10^-5;
rhs = Epsilon_dchost *pi /qe *(hbar *vF/kBT)^2;
```

```
syms u

g = polylog(2,-exp(-u))- polylog(2,-exp(u));
f = g - (rhs*EdcVm);
d_f = diff(f);
xnew = u - (f/d_f);

x(1) = double(subs(xnew,u,3));
for i = 2:100
    x(i) = double(subs(xnew,u,x(i-1)));

    if abs(1-x(i)/x(i-1)) < delta
        break
    end

end
mu_ceV = x(i)*kBT/qe;  %Chemical Potential in eV

%%
mu_cV = mu_ceV*qe;

%surface conductivity
sigma_o = (qe^2)*kBT*Tau/(pi*hbar^2)*(mu_cV/kBT+2*log(exp(-mu_cV/kBT)+1));
sigma = sigma_o/(1+1j*Omega*Tau);

Zs = 1/sigma;

Conductivity = sigma./dgr_m;
```

APPENDIX B
PUBLICATIONS

- E. Chong, S. Clemens, M. F. Iskander, Z. Yun, J. J. Brown, and M. Nakamura, "Using genetic programming to achieve high broadband absorptivity metamaterial in compact radar band (1–11 ghz) without lossy materials," in *2022 IEEE International Symposium on Antennas and Propagation and USNC-URSI Radio Science Meeting (AP-S/URSI)*, pp. 1364–1365, 2022
- S. Clemens, E. Chong, M. F. Iskander, Z. Yun, J. Brown, T. Ray, M. Nakamura, and D. Nekoba, "Hybrid genetic programming designed laser-induced graphene based absorber," in *2022 IEEE International Symposium on Antennas and Propagation and USNC-URSI Radio Science Meeting (AP-S/URSI)*, pp. 1084–1085, 2022

BIBLIOGRAPHY

[1] J. Rayno, M. F. Iskander, and M. H. Kobayashi, "Hybrid Genetic Programming With Accelerating Genetic Algorithm Optimizer for 3-D Metamaterial Design," *IEEE Antennas and Wireless Propagation Letters*, vol. 15, pp. 1743–1746, 2016.

[2] S. Clemens, M. F. Iskander, Z. Yun, and J. Rayno, "Hybrid Genetic Programming for the Development of Metamaterials Designs With Improved Characteristics," *IEEE Antennas and Wireless Propagation Letters*, vol. 17, pp. 513–516, Mar. 2018.

[3] C. Xu, B. Wang, Y. Pang, J. Wang, M. Yan, W. Wang, A. Wang, J. Jiang, and S. Qu, "Hybrid Metasurfaces for Infrared-Multiband Radar Stealth-Compatible Materials Applications," *IEEE Access*, vol. 7, pp. 147586–147595, 2019.

[4] M. Li, B. Muneer, Z. Yi, and Q. Zhu, "A Broadband Compatible Multispectral Metamaterial Absorber for Visible, Near-Infrared, and Microwave Bands," *Advanced Optical Materials*, vol. 6, no. 9, p. 1701238, 2018.

[5] S. Clemens, E. Chong, M. F. Iskander, Z. Yun, J. Brown, T. Ray, M. Nakamura, and D. Nekoba, "Hybrid genetic programming designed laser-induced graphene based absorber," in *2022 IEEE International Symposium on Antennas and Propagation and USNC-URSI Radio Science Meeting (AP-S/URSI)*, pp. 1084–1085, 2022.

[6] A. Li, S. Singh, and D. Sievenpiper, "Metasurfaces and their applications," *Nanophotonics*, vol. 7, pp. 989–1011, June 2018.

[7] P. Yu, L. V. Besteiro, Y. Huang, J. Wu, L. Fu, H. H. Tan, C. Jagadish, G. P. Wiederrecht, A. O. Govorov, and Z. Wang, "Broadband Metamaterial Absorbers," *Advanced Optical Materials*, vol. 7, no. 3, p. 1800995, 2019.

[8] A. El Assal, H. Breiss, R. Benzerga, A. Sharaiha, A. Jrad, and A. Harmouch, "Toward an Ultra-Wideband Hybrid Metamaterial Based Microwave Absorber," *Micromachines*, vol. 11, p. 930, Oct. 2020.

[9] T. H. Nguyen, S. T. Bui, T. T. Nguyen, T. T. Nguyen, Y. Lee, M. A. Nguyen, and D. L. Vu, "Metamaterial-based perfect absorber: polarization insensitivity and broadband," *Advances in Natural Sciences: Nanoscience and Nanotechnology*, vol. 5, p. 025013, May 2014.

[10] F. Ding, Y. Cui, X. Ge, Y. Jin, and S. He, "Ultra-broadband microwave metamaterial absorber," *Applied Physics Letters*, vol. 100, p. 103506, Mar. 2012.

[11] N. Lee, J.-S. Lim, I. Chang, D. Lee, and H. H. Cho, "Transparent Metamaterials for Multispectral Camouflage with Thermal Management," *International Journal of Heat and Mass Transfer*, vol. 173, p. 121173, July 2021.

[12] S. Huang, Q. Fan, C. Xu, B. Wang, J. Wang, B. Yang, C. Tian, and Z. Meng, "A visible-light-transparent camouflage-compatible flexible metasurface for infrared–radar stealth applications," *Journal of Physics D: Applied Physics*, vol. 54, p. 015001, Jan. 2021.

[13] T. Kim, J.-Y. Bae, N. Lee, and H. H. Cho, "Hierarchical Metamaterials for Multispectral Camouflage of Infrared and Microwaves," *Advanced Functional Materials*, vol. 29, no. 10, p. 1807319, 2019.

[14] X. Feng, X. Xie, M. Pu, X. Ma, Y. Guo, X. Li, and X. Luo, "Hierarchical metamaterials for laser-infrared-microwave compatible camouflage," *Opt. Express*, vol. 28, pp. 9445–9453, Mar 2020.

[15] Y. Yang, Y. Song, and S. Fan, "Design of a metamaterial absorber based on resistive film structure," *AIP Conference Proceedings*, vol. 1971, no. 1, p. 020008, 2018.

[16] "Graphene Synthesis, Properties, And Applications – Cheap Tubes."

[17] A. Alex-Amor, A. Palomares-Caballero, and C. Molero, "3-D Metamaterials: Trends on Applied Designs, Computational Methods and Fabrication Techniques," *Electronics*, vol. 11, p. 410, Jan. 2022.

[18] G. C. Huang, S. Clemens, M. F. Iskander, and Z. Yun, "Analysis of GP-designed metamaterial using equivalent circuit model and Prony's method," *Electromagnetics*, vol. 41, pp. 381–392, Aug. 2021.

[19] T. J. Cui, M. Q. Qi, X. Wan, J. Zhao, and Q. Cheng, "Coding metamaterials, digital metamaterials and programmable metamaterials," *Light: Science & Applications*, vol. 3, pp. e218–e218, Oct. 2014.

[20] T. J. Cui, S. Liu, and L. Zhang, "Information metamaterials and metasurfaces," *Journal of Materials Chemistry C*, vol. 5, pp. 3644–3668, Apr. 2017.

[21] J. Rayno, *Development and Application of Genetic Programming in the Design and Optimization of Ultra-Wideband 3D Metamaterials.* Thesis, [Honolulu] : [University of Hawaii at Manoa], [May 2016], May 2016.

[22] S. Bringhurst and M. Iskander, "Thin sample dielectric properties measurement using open-ended coaxial probes and FDTD calculations," in *IEEE Antennas and Propagation Society International Symposium. 1995 Digest*, vol. 4, pp. 1844–1847 vol.4, June 1995.

[23] S. Clemens, G. C. Huang, M. F. Iskander, and Z. Yun, "Measurement of Hybrid Genetic Programming Synthesized Artificial Magnetic Conductors," in *2019 IEEE International Symposium on Antennas and Propagation and USNC-URSI Radio Science Meeting*, pp. 1403–1404, July 2019. ISSN: 1947-1491.

[24] J. D. Kraus, *Antennas.* McGraw-Hill electrical and electronic engineering series, New York: McGraw-Hill, 1st ed. ed., 1950.

[25] R. Rudrapati, "Graphene: Fabrication methods, properties, and applications in modern industries," in *Graphene Production and Application* (S. Ameen, M. S. Akhtar, and H.-S. Shin, eds.), ch. 2, Rijeka: IntechOpen, 2020.

[26] T. Wei, F. Hauke, and A. Hirsch, "Evolution of graphene patterning: From dimension regulation to molecular engineering," *Advanced Materials*, vol. 33, no. 45, p. 2104060, 2021.

[27] T.-S. D. Le, H.-P. Phan, S. Kwon, S. Park, Y. Jung, J. Min, B. J. Chun, H. Yoon, S. H. Ko, S.-W. Kim, and Y.-J. Kim, "Recent advances in laser-induced graphene: Mechanism, fabrication, properties, and applications in flexible electronics," *Advanced Functional Materials*, vol. 32, no. 48, p. 2205158, 2022.

[28] F. Wang, K. Wang, B. Zheng, X. Dong, X. Mei, J. Lv, W. Duan, and W. Wang, "Laser-induced graphene: preparation, functionalization and applications," *Materials Technology*, vol. 33, no. 5, pp. 340–356, 2018.

[29] G. W. Hanson, "Dyadic green's functions for an anisotropic, non-local model of biased graphene," *IEEE Transactions on Antennas and Propagation*, vol. 56, no. 3, pp. 747–757, 2008.

[30] X. Huang, Z. Hu, and P. Liu, "Graphene based tunable fractal Hilbert curve array broadband radar absorbing screen for radar cross section reduction," *AIP Advances*, vol. 4, p. 117103, Nov. 2014.

[31] A. Lakhtakia, "Single-layer graphene," 2019.

[32] H. Bin Zhang, P. Heng Zhou, L. Wei Deng, J. Liang Xie, D. Fei Liang, and L. Jiang Deng, "Frequency-dispersive resistance of high impedance surface absorber with trapezoid-coupling pattern," *Journal of Applied Physics*, vol. 112, no. 1, p. 014106, 2012.

[33] N. Dixit and S. P. Singh, "Laser-Induced Graphene (LIG) as a Smart and Sustainable material to Restrain Pandemics and Endemics: A Perspective," *ACS Omega*, vol. 7, pp. 5112–5130, Feb. 2022.

[34] E. Chong, S. Clemens, M. F. Iskander, Z. Yun, J. J. Brown, and M. Nakamura, "Using genetic programming to achieve high broadband absorptivity metamaterial in compact radar band (1–11 ghz) without lossy materials," in *2022 IEEE International Symposium on Antennas and Propagation and USNC-URSI Radio Science Meeting (AP-S/URSI)*, pp. 1364–1365, 2022.